ChemElectroChem

Research Article
doi.org/10.1002/celc.202400230

Chemistry Europe
European Chemical Societies Publishing

www.chemelectrochem.org

Corn Husk Derived Activated Carbon/Siloxene Composite Electrodes based Symmetric Supercapacitor with High Energy Density and Wide Temperature Tolerance

Kiran Kumar Reddy Reddygunta,[a] Lidija Šiller,[b] and Aruna Ivaturi*[a]

In the present work, novel composite material comprising of corn husk derived activated carbon and siloxene nanosheets have been explored as new class of multicomponent electrode material for fabricating high energy density supercapacitors with wide temperature tolerance. The activated carbon obtained from corn husk (ACH–900) with high surface area and pore volume acts as an ideal framework for hosting siloxene nanosheets (S) that allows the overall siloxene–corn husk derived activated carbon (ACH–900/S) composite to deliver excellent electrochemical performance. The as-prepared ACH–900/S composite electrode exhibited a high specific capacitance of 415 $F g^{-1}$ at 0.25 $A g^{-1}$ and retained 73.4% of its initial capacitance even at a high current density of 30 $A g^{-1}$ in 1 M Na_2SO_4 electrolyte. In addition, the symmetric supercapacitor assembled with "acetonitrile/water-in-salt (AWIS)" electrolyte exhibited an energy density of 57.2 $W h kg^{-1}$ at 338 $W kg^{-1}$ with a cyclic stability of 92.8% after 10000 cycles at 5 $A g^{-1}$ current density. Besides, the fabricated ACH–900/S supercapacitor can operate over wide temperature range from 0 to 100 °C. This work opens up new frontiers to develop low-cost safe supercapacitors with wide temperature tolerance and excellent electrochemical performance.

1. Introduction

Due to the expanding markets for electric vehicles and the rapid development of portable/wearable consumer electronics, electrochemical energy storage systems have been tested under various protocols and regulations to maintain higher standards and regulations. Electrochemical supercapacitors, which deliver high power density than batteries and store more energy than traditional capacitors, are currently being investigated for widespread applications in electric vehicles, power electronics for backup storage and peak power savings. Due to the rapid advancement in supercapacitor field, supercapacitors that can survive a wide temperature range are currently in high demand for numerous applications, including hybrid electric vehicles, portable electronic gadgets, and aerospace power sources.[1,2]

Due to its quick charge/discharge capability, high power density, and extended cycle life, biomass activated carbon-based supercapacitors have recently gained a lot of attention among various electrochemical energy storage devices.[3,4] Although activated carbon made from biomass has many benefits, including being widely available, inexpensive, environmentally friendly, having an abundance of surface functional groups, and tunable surface properties, their low energy density prevents them from being used in a variety of applications, including portable devices, and electric vehicles.[5,6] According to the energy density equation, $E_d = 0.5*C\Delta V^2$, the energy density can be enhanced by increasing the specific capacitance (C) of the activated carbon electrodes.[7] The specific capacitance of the biomass activated carbon electrodes can be increased by increasing the specific surface area (S) because of higher amount of charge accumulation on the electrode surface.[8] However, high surface area alone is not sufficient for high capacitance because not all the pores on the surface are electrochemically accessible. Hence, it is crucial to produce activated carbon with an 'open' pore network because the open pore network facilitates the rapid transportation of electrolyte inside the porous network, and makes the surface more electrochemically accessible. Recent investigations proved that the electrochemical performance of biomass activated carbon electrodes can be improved by introducing the two-dimensional (2D) materials such as graphene and MXene into the porous carbon framework.[9,10] The introduction of 2D materials creates large openness inside the porous carbon framework which allows more efficient ionic transport inside the porous network thus increasing the specific capacitance of the biomass activated carbon electrodes.[9] For example, Laura et al.[10] combined reduced graphene oxide (rGO) with grape seed residue derived activated carbon which delivered a high

[a] K. K. R. Reddygunta, Dr. A. Ivaturi
Smart Materials Research and Device Technology (SMaRDT) Group,
Department of Pure and Applied Chemistry,
University of Strathclyde, Thomas Graham Building,
Glasgow, G1 1XL, UK
E-mail: aruna.ivaturi@strath.ac.uk

[b] Prof. L. Šiller
School of Engineering,
Newcastle University,
Newcastle upon Tyne,
NE1 7RU, UK

Supporting information for this article is available on the WWW under https://doi.org/10.1002/celc.202400230

specific capacitance of 260 F g^{-1} at 1 mA cm^{-2} current density in aqueous H_2SO_4 electrolyte. Furthermore, introduction of rGO into the activated carbon reduced the internal resistance of composite supercapacitors by around 72% and also enhanced the rate capability. The presence of conductive rGO layers inside the porous carbon network enhances the connective pathways between the porous activated carbon particles thereby reducing the internal resistance and increases the rate capability of the composite electrodes.[10] On the other hand, Yi et al.[9] utilized hydrothermal technique to decorate MXene/rGO nanosheets on the surface of pleurotus eryngii derived activated carbon [MG@AC-3]. The as-prepared MG@AC-3 composite with interconnected porous network exhibited high surface area of 1174.4 $m^2 g^{-1}$, and delivered a specific capacitance of 442 F g^{-1} which is higher that the porous activated carbon (283 F g^{-1}) at 2 mV s^{-1} scan rate in 3 M H_2SO_4 electrolyte. According to the authors, the presence of MXene/rGO is favourable for rapid ionic transmission inside the porous carbon network and activated carbon reduces the restacking of $Ti_3C_2T_x$ and rGO nanosheets. Similarly, Wei et al.[11] prepared CPCM/MXene sandwich structure like composite by introducing $Ti_3C_2T_x$ MXene into chitosan-based porous carbon microsphere (CPCM). The combined effect of MXene and CPCM endowed the composite CPCM/MXene electrode with a high specific capacitance of 362 F g^{-1} at 0.5 A g^{-1} current density and cycling stability of 93.87% at 10 A g^{-1} current density in 1 M H_2SO_4 electrolyte after 10000 cycles. These results suggest that the electrochemical performance of biomass activated carbon materials can be enhanced by introducing 2D materials. Thus, in the present study, corn husk derived activated carbon (ACH) has been decorated with 2D Siloxene (S) sheets using topochemical reaction mechanism.

Siloxene (a 2D material comprising silicon sheets functionalized with oxygenated groups) is considered as an attractive electrode material for future energy storage application because of its high theoretical capacity of 4200 mAh g^{-1}.[12,13] Siloxene sheets are prepared via topochemical etching of Ca from calcium silicide ($CaSi_2$) using hydrochloric acid (HCl) and it is considered as an exciting material due to their direct bandgap and 2D structure made up of Si chains connected to oxygen, hydrogen, and hydroxyl functional groups with rich structural stability. Krishnamoorthy et al.[14] fabricated a symmetric supercapacitor with 2D siloxene sheet electrodes which showed a specific capacitance of 2.18 mF cm^{-2} (8.1 F g^{-1}) in 0.5 M tetraethylammonium tetrafluoroborate electrolyte. Although, the device showed excellent electrochemical performance, the siloxene sheets tend to aggregate resulting in rapid decay in capacitance hindering its practical application.[12,13] One of the remedial measures to overcome this issue is to decorate the siloxene sheets on the surface/inside the porous biomass activated carbon framework. This inspired us to develop 2D siloxene sheets/corn husk derived activated carbon (ACH/S) composite for the first time as a new type of hybrid electrode for supercapacitor. The siloxene sheets embedded fills the large pores and cover the surface of corn husk derived activated carbon, creating an open porous framework for effectively accelerating the ion transportation.

In addition to electrode materials, electrolyte which facilitates the ionic conduction between two electrodes is an integral part of supercapacitors which determines the overall performance of supercapacitors.[15,16] Ionic liquids and organic electrolytes offer wider electrochemical potential windows (> 3.0 V) than aqueous electrolytes, which significantly enhances the energy density of the supercapacitors.[17,18] However, organic electrolytes pose a safety risk due to their flammability nature, and ionic liquids have higher viscosity and lesser conductivity when compared to organic electrolytes, particularly at low temperatures. Furthermore, ionic and organic electrolytes are highly expensive and sensitive to moisture, necessitating specialized purification and ultra-dry manufacturing techniques.[19,20] Aqueous electrolytes, on the other hand, are intrinsically safe and simple to use. However, their practical application is limited by electrochemical stability window of water (pure water decomposes at 1.23 V).[15,19] Therefore, careful design as well as optimization of new electrolyte systems that can deliver wider potential windows and possess extreme temperature tolerance is of paramount importance to develop next-generation supercapacitors with excellent electrochemical performance and extreme safety standards.

Distinguished from traditional aqueous electrolytes, superconcentrated "water in salt" (WIS) electrolytes are labelled as a new class of electrolyte systems, since first proposed by Suo et al. in 2015.[20,21] WIS electrolytes have been employed in activated carbon-based supercapacitors because of their remarkably wide potential windows due to the significantly reduced water content as well as the effective limitation of chemical activity of water molecules.[22–24] For instance, the voltage of the N, O co-doped porous carbon-based supercapacitor using 7 m lithium bis(trifluoromethanesulfonyl) imide [7 m LiTFSI where m = mol/kg] WIS electrolyte reached up to 2.2 V with an excellent energy density of 30.4 W h kg^{-1}.[25] Hasegawa et al.[24] prepared a symmetric supercapacitor with porous activated carbon monolith electrodes and 18.7 m LiTFSI WIS electrolyte. The as-prepared supercapacitor demonstrated 2.4 V potential window with an overall energy density of 24 W h kg^{-1} at 0.48 kW kg^{-1} in 18.7 m LiTFSI WIS electrolyte.[24] Similarly, Xu et al.[7] investigated the temperature [from −20 to 100 °C] dependent performance of rose-petal derived carbon (RPC) electrode supercapacitor in 20 m LiTFSI WIS electrolyte. The as-prepared device showed a working potential of 2.4 V and excellent temperature tolerance with an energy density of 44 W h kg^{-1} at 564 W kg^{-1} power density at 60 °C. Their work established a protocol for using WIS electrolytes in carbon-based supercapacitors, thereby advancing the practical application of supercapacitors over a wide temperature range. Although LiTFSI based WIS outperforms standard aqueous electrolytes, their drawbacks are unsatisfactory: expensive cost due to high dosage of imide-based salts, reduced ionic conductivity, and high viscosity limit their future broad usage.[26] Meanwhile, sodium perchlorate ($NaClO_4$) based WIS has garnered immense attention because of its low cost, low viscosity and high conductivity.[26,27] For example, Pang et al.[23] fabricated a symmetric supercapacitor using 17 m $NaClO_4$ WIS electrolyte and ground grain hull derived activated carbon

electrodes which showed a capacitance 59 F g^{-1} at 0.5 A g^{-1} in 2.4 V potential window and an excellent energy density of 47.2 W h kg^{-1}. However, the excessive high salt concentration results in low conductivity and high viscosity of electrolytes, which negatively affects device performance.[28–30] In order to address this drawback, Dou et al.[27,31] developed a "acetonitrile/ water in salt" (AWIS) based hybrid electrolyte system which can offer improved conductivity, decreased viscosity, and a wider temperature tolerance. Their hybrid $NaClO_4$ based AWIS electrolyte with a salt-to-water-to-acetonitrile molar ratio of 1/1.5/2.4 showed a wide potential window (3.16 V) while maintaining high ionic conductivity (41.2 mS cm^{-1}), excellent wettability, and flame-retardant properties.[27] They adopted similar strategy to prepare 5 m LiTFSI based AWIS electrolyte where the capacitance of assembled carbon based supercapacitor is 2.4 times greater than that of pure 21 m LiTFSI based WIS electrolyte. These findings showed that the addition of acetonitrile enhanced the conductivity of the electrolyte, decreased its viscosity, and increased the temperature tolerance over which it could be used. More significantly, it also preserved the wide potential window, and non-flammability of the original WIS electrolyte. Hence, in the present research we utilized the concept of hybrid AWIS electrolyte developed by Dou et al.[27] [8 m $NaClO_4$/ $(H_2O)_{1.5}(AN)_{2.4}$] to fabricate a symmetric supercapacitor with excellent electrochemical performance and wide temperature tolerance.

Herein, we report the fabrication of symmetric supercapacitor with siloxene–corn husk derived activated carbon (ACH–900/S) composite electrode and AWIS electrolyte, i.e. cheap sodium perchlorate ($NaClO_4$) salt mixed with water/acetonitrile solvents. For this purpose, corn husk was selected as a biomass precursor for producing high surface area (1508 m^2 g^{-1}) porous activated carbon which delivered a specific capacitance of 279 F g^{-1}. Furthermore, 2D siloxene (S) sheets have been introduced into the corn husk derived activated carbon (ACH–900) to enhance the electrochemical performance. The as-prepared ACH–900/S composite possess a unique morphology where the siloxene sheets fill the pores of ACH–900, effectively accelerating the ion transportation inside the porous carbon frame work, whereas the interconnected pore network can minimize the adverse effect of the aggregation and restacking of siloxene sheets. Benefitting from the synergistic effect of porous carbon (ACH–900) and 2D siloxene (S), the ACH–900/S composite electrode demonstrated a high specific capacitance of 415 F g^{-1} at 0.25 A g^{-1} in 1 M Na_2SO_4 electrolyte. Subsequently, a symmetric supercapacitor is fabricated with ACH–900/S composite electrode and 8 m $NaClO_4$/ $(H_2O)_{1.5}(AN)_{2.4}$ AWIS electrolyte. The device exhibited an operating potential of 3.0 V with high energy density of 57.2 W h kg^{-1} at 338 W kg^{-1}, capacitance of 92.8% after 10000 cycles at 5 A g^{-1} current density and excellent temperature tolerance.

Experimental Section

Materials and Methods

Materials and Reagents

Corn was purchased from a local supermarket in Glasgow, UK. Potassium bicarbonate ($KHCO_3$, 99.7%), sodium sulfate (Na_2SO_4, 99%), sodium perchlorate ($NaClO_4$, 99%), calcium silicide ($CaSi_2$), polyvinylidene fluoride (PVDF) binder, 1-methylpyrrolidone from Sigma-Aldrich. Acetonitrile and hydrochloric acid (HCl, 37%) was obtained from Fisher Scientific. All the chemicals were used as received without any purification.

Preparation of Activated Carbon from Corn Husk

The initial step of this research was to synthesize activated carbon from corn husk. For this purpose, husk was separated and dried at 100 °C for 48 h. The corn husk was pulverized to powder using a Fritsch ball mill and sieved using a 100 μm mesh to collect fine powder of particle size ≤ 100 μm. The obtained powder was stored inside a hot air oven at 100 °C until used.

Corn husk based activated carbon was prepared via carbonization followed by activation of carbonized materials. Firstly, the pulverized powder from corn husk was placed in a horizontal tube furnace and ramped from room temperature to 400 °C at 10 °C min^{-1} under nitrogen flow and kept at this temperature for 2 h to allow the carbonization process to take place.[32] After 2 h, the furnace was turned off and allowed to cool naturally. Next, the carbonized powder was thoroughly ground with $KHCO_3$ (mass ratio of $KHCO_3$/carbonized powder is 3:1) in an agate mortar. Subsequently, the mixture was annealed at 800–1000 °C (heating rate: 10 °C min^{-1}) for 2 h under a nitrogen atmosphere.[8] Finally, the activated samples were sufficiently washed with 1 M HCl and deionized water several times until the pH of the filtrate becomes neutral. The activated samples were then washed with ethanol and then dried at 100 °C overnight. The as-prepared samples were denoted as ACH–T, where T indicates the activation temperature.

Preparation of Siloxene/ ACH–900 Composites

AC husk/Siloxene are synthesized by topochemical etching of Ca from $CaSi_2$ in the presence of ACH–900 suspended in ice-cold HCl. Initially, 100 mg of ACH–900 sample was dispersed in 100 mL concentrated HCl under stirring at ice cold temperature. Later, 100 mg of thoroughly grounded $CaSi_2$ powder was gradually added to the above mixture and magnetically stirred for 24 h at ambient temperature. After 24 h, black colored solution was obtained which is washed with deionized water, ethanol several times until a neutral pH is obtained. As a control, pure siloxene was also prepared in the same strategy without the addition of ACH–900. The as-prepared samples were denoted as S, ACH–900/S where S correspond to pure siloxene and ACH–900/S correspond to ACH–900/Siloxene composite.

Material Characterizations

The crystalline nature of the synthesized materials was examined by X-ray diffraction (XRD) using a Bruker D2 Phaser system using monochromatic CuK_α radiation ($\alpha = 1.5406$ Å). The samples were scanned in the range 5–80 degrees and an increment of 0.04 on the 2θ scale. The substrates were set to a rotation speed of 8 degrees per min throughout the measurements. The specific surface area (SSA) and pore volume of the as prepared samples

were analysed via Brunauer-Emmett-Teller (BET) and Non-Linear-Density-Functional-theory (NLDFT) method using a Micrometrics ASAP 2020 porosity analyzer at 77 K. Prior to the SSA investigations, the samples were degassed for 3 h in a dynamic vacuum at a temperature of 300 °C. To study the defective/graphitic nature of the as-prepared samples, Raman spectra were measured using a WiTec Raman microscope with an excitation wavelength of 532 nm within a spectral range of 500 to 3500 cm^{-1}. The laser power was set to 2.69 mW using 100X objective lens with an acquisition time of 10 s. Calibration was performed using a silicon standard (520 cm^{-1}). Samples were analysed under the microscope and five different spectra were recorded from different parts of the sample, and averaged to gain a representative spectrum, using a MATLAB script. The morphological features of samples were obtained using FEI Quanta 250 FEGSEM using 5 kV electron beam. EDX spectra were acquired from the full area of the corresponding 1000X magnification image using a 20 kV electron beam. X-ray photoemission spectroscopy (XPS) analysis was conducted using a Thermo Scientific K-alpha X-ray Photoelectron Spectrometer™ (Thermo Scientific, East Grinstead, UK). High resolution photoemission spectra of specific element regions (C1s, O1s, N1s) were collected at 40 eV pass energy of hemispherical electron analyzer with 0.05 eV energy step size. Spectra were acquired using a monochromatic Al Kα x-ray source with an output energy of 1486.6 eV with a maximum x-ray beam spot size of 400 μm. Surface charge compensation was obtained with a low energy dual-beam electron/ion flood gun. All XPS and Raman spectra were normalized and Voigt fitting was used for the deconvolution of the spectra with Fityk software.

Electrode Preparation for Three Electrode and two Electrode Measurements

For the three electrode measurements, a homogenous slurry was prepared by mixing electroactive material [ACH–T, S, ACH–900/S] and PVDF in the weight ratio of 90:10 along with few drops of 1-methylpyrrolidine. The slurry was then coated on 1 cm^2 area onto a stainless-steel mesh (3 cm×1 cm) using doctor blading and then dried at 80 °C for 2 h. For preparing electrodes with 2D materials (MXene, Siloxene, Bismuthene), nearly 10% of conductive additives like activated carbon, carbon black, graphite/graphene is added to improve the conductivity of the electrodes.[14,33,34] Thus in this study, Siloxene (S) electrodes were prepared by mixing as synthesized siloxene, ACH–900 and PVDF in the weight ratio of 80:10:10, along with few drops of 1-methylpyrrolidine. The slurry was then coated on 1 cm^2 area onto a stainless-steel mesh (3 cm×1 cm) using doctor blading and then dried at 80 °C for 2 h. The stainless-steel mesh has an aperture of 0.026 mm and wire diameter of 0.025 mm. The approximate weight of the activated carbon on the stainless steel mesh electrodes was as follows: ACH–800 = 2.8 mg, ACH–900 = 2.5 mg, ACH–1000 = 2.5 mg, Siloxene (S) = 2.9 mg, and ACH–900/S = 2.4 mg.

For two electrode measurements, electrochemical experiments were carried out with Swagelok cell, using electroactive materials [ACH–900, S, and ACH–900/S] as working electrodes and stainless-steel mesh as current collector and 8 m $NaClO_4$ acetonitrile/water-in-salt (AWIS) electrolyte [8 m $NaClO_4/(H_2O)_{1.5}(AN)_{2.4}$][27] as the electrolyte. For this purpose, electroactive materials [ACH–900, S, ACH–900/S] and PVDF were mixed in 90:10 ratio along with few drops of 1-methylpyrrolidone to form a slurry. The slurry was then coated on two circular shaped stainless-steel mesh current collectors (14 mm diameter) and dried inside the oven at 80 °C for 3 h. The electrodes were sandwiched with 8 m $NaClO_4$ AWIS soaked FB59017 filter paper separator (diameter: 14 mm) in a two electrode Swagelok cell assembly as shown in supporting information Figure S5.

Electrochemical Measurements

The electrochemical behavior of ACH–T, S, ACH–900/S was studied by cyclic voltammetry (CV), galvanostatic charge discharge (GCD) and electrochemical impedance spectroscopy (EIS) techniques. All CV, GCD and EIS tests were carried out at room temperature using an Autolab PGSTAT 302N potentiostat/galvanostat with FRA32 M module. For a typical three electrode measurement, activated carbon coated stainless steel mesh, Ag/AgCl and platinum wire were used as the working, reference and counter electrodes, respectively. 1 M Na_2SO_4 was used as the electrolyte for three electrode measurements here.

The specific capacitance C_s (F g^{-1}) was estimated from the galvanostatic charge-discharge measurements in the three electrode configuration by means of Equation (1):[8]

$$C_s = \frac{I \times \Delta t}{m \Delta V} \tag{1}$$

where I represent the current (in ampere), Δt is the discharge time after IR drop, m is the mass of the active material on the electrode and ΔV is the potential window after IR drop.

In two-electrode configuration, the total capacitance C_t (F g^{-1}) of the device, energy density E_d (W h kg^{-1}) and power density P_d (W kg^{-1}), were calculated from galvanostatic charge-discharge measurements by means of equations (2–5):[35,36]

$$C_t = \frac{I}{M\left(\frac{\Delta V}{\Delta t}\right)} \tag{2}$$

$$C_{es} = 4 \times C_t \tag{3}$$

$$E_d = \frac{1}{2}\frac{C_t \times \Delta V^2}{3.6} \tag{4}$$

$$P_d = \frac{E_d \times 3600}{\Delta t} \tag{5}$$

where M is the total weight of active material within the two electrodes, ($\Delta V/\Delta t$) is the slope of the discharge curve.

Temperature dependent measurements were carried out by placing the Swagelok cell inside the hot air oven. For low temperature measurements (0 °C), the Swagelok cell was placed inside the polystyrene thermocol box containing solid ice cubes. Temperature of the Swagelok cell device was additionally monitored by digital thermometer coupled with a thermal sensor connected to the device.

2. Results and Discussions

2.1. XRD Studies

XRD studies were carried out for the as-prepared ACH–T, S, ACH–900/S samples in order to analyze their crystal structure. As shown in Figure 1 (a), ACH–T samples prepared at different

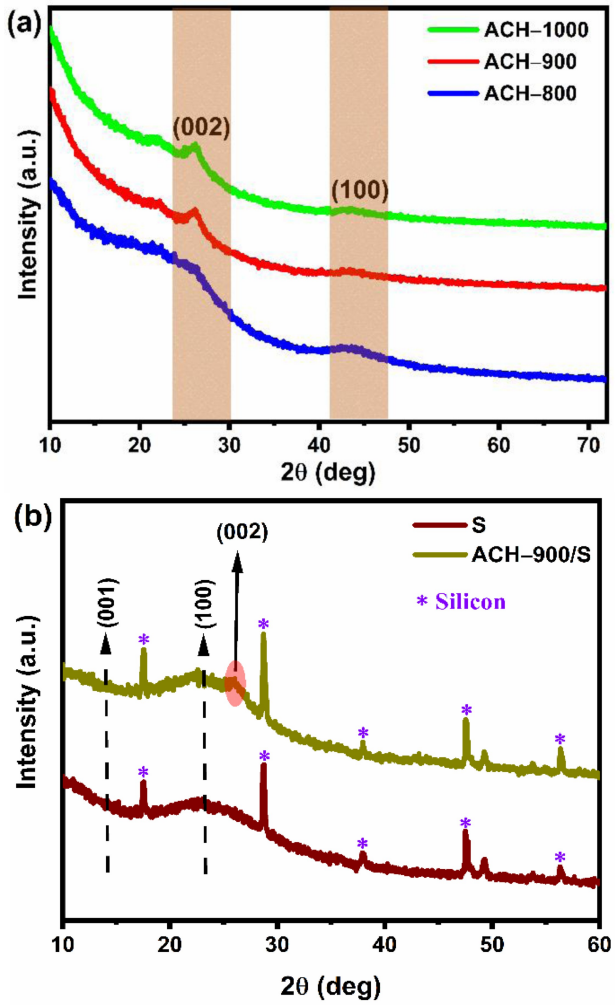

Figure 1. (a) XRD patterns of ACH–T samples (b) XRD patterns of S, ACH–900/S samples.

temperatures displays the presence of a broad peak at ~26.1° and a low intensity peak at ~43.6° corresponding to (002) and (100) planes of amorphous carbon with partially graphitic features.[8,37] The presence of micropores in the ACH–T samples is indicated by the high intensity in the low angle region, which is compatible with the N_2 sorption data shown in Figure 2.[38]

Figure 1 (b) presents the XRD graph of pure siloxene (S) and the composite ACH–900/siloxene (ACH–900/S) composite samples. The XRD pattern of S and ACH–900/S sample displayed broad diffraction peaks (indicated by dashed arrow) centred at ~13.5° and ~24° corresponds to (001) and (100) planes of siloxene sheets.[39,40] Beside these, sharper peaks were observed in the S and ACH–900/S XRD pattern (indicated by *) corresponding to the unavoidable impurity (crystalline silicon) in $CaSi_2$.[39,41] Also, there is peak at 49.3° in both the samples corresponding to the residual $CaSi_2$. Apart from the siloxene peaks, a broad peak (indicated by solid arrow) at ~26.1° is visible in ACH–900/S composite which corresponds to the amorphous carbon structure.

2.2. N_2 Adsorption/Desorption Studies

The porosity of the ACH–T, S, ACH–900/S samples are measured by the N_2 adsorption-desorption isotherms at 77 K and the results are shown in Figure 2. Figure 2 (a) shows the N_2 adsorption-desorption isotherms of activated carbon (ACH–T) samples obtained from corn hush biomass at different activation temperatures. Figure 2 (a) shows that ACH–T samples have Type IV isotherms with an H4 hysteresis loop, indicating the presence of hierarchical porous structures with dominant meso-pores.[42,43] The adsorption isotherms of ACH–T samples show steep uptake tendency at lower P/P_0 values ($P/P_0 < 0.1$) indicating that the samples possess micropores. Furthermore, the modest uptake in adsorption line at $0.9 < P/P_0 < 1.0$ indicates the co-existence of micro-, meso- and macropores.[44] The adsorption/desorption isotherms indicate that the synthesized ACH–T materials contain interconnected porous network with a mix of micro- and mesoporous structures. Furthermore, the amount of N_2 adsorbed increases with increasing activation temperature from 800 to 900 °C, but decreases when the temperature is elevated to 1000 °C. This indicates that the porosity increases with increasing activation temperature until 900 °C, at which point the network begins to collapse, resulting in a decrease in surface area of the sample activated at 1000 °C. The specific surface area (SSA) values of corn husk based activated carbon samples are in the order of ACH–900 ($1508\ m^2g^{-1}$) > ACH–1000 ($1310\ m^2g^{-1}$) > ACH–800 ($1152\ m^2g^{-1}$) indicating greater number of mesopores have evolved in the case of sample activated at 900 °C. Furthermore, the pore size distribution (PSD) plot shown in the inset of Figure 2 (b) indicates that the pores are predominantly distributed within a narrow range of 2–5 nm. Table S1 shows the pore characteristics of the as-prepared corn hush activated carbons at different activation temperatures. According to Table S1 and the adsorption/desorption isotherm curves, all of the samples had mesoporous structures with an average pore size of 2–5 nm. However, the ACH–900 sample possessed a high SSA ($1508\ m^2g^{-1}$) and a higher SSAmeso/SSAT value (57.3 %), which represents the existence of a large number of mesopores in the as-synthesized sample. The large SSA and pore volume may not only endow the ACH–900 with remarkable electrochemical performance but also acts as an excellent template for the growth of siloxene nanosheets on it.

Figure 2 (c) and 2 (d) shows the nitrogen adsorption/desorption isotherms and PSD plots for the as-prepared siloxene (S) and ACH–900/S composite materials. Figure 2 (c) shows that S and ACH–900/S composite materials' isotherms are associated with type IV with H3 hysteresis. The N_2 adsorption curves of the S and ACH900/S composite are relatively steep in the low-pressure region, as illustrated in Figure 2 (c), which suggests that there are micropores present. The sharp rising hysteresis loop at the relative pressure between 0.9 and 1.0 validates the mesoporous property of S and ACH–900/S composite materials.[39,41] The SSAs of S and ACH–900/S were examined to be 32 and $692\ m^2g^{-1}$ respectively. From the N_2 adsorption analysis, it can be observed that the ACH–900/S composite possess smaller SSA, pore volume

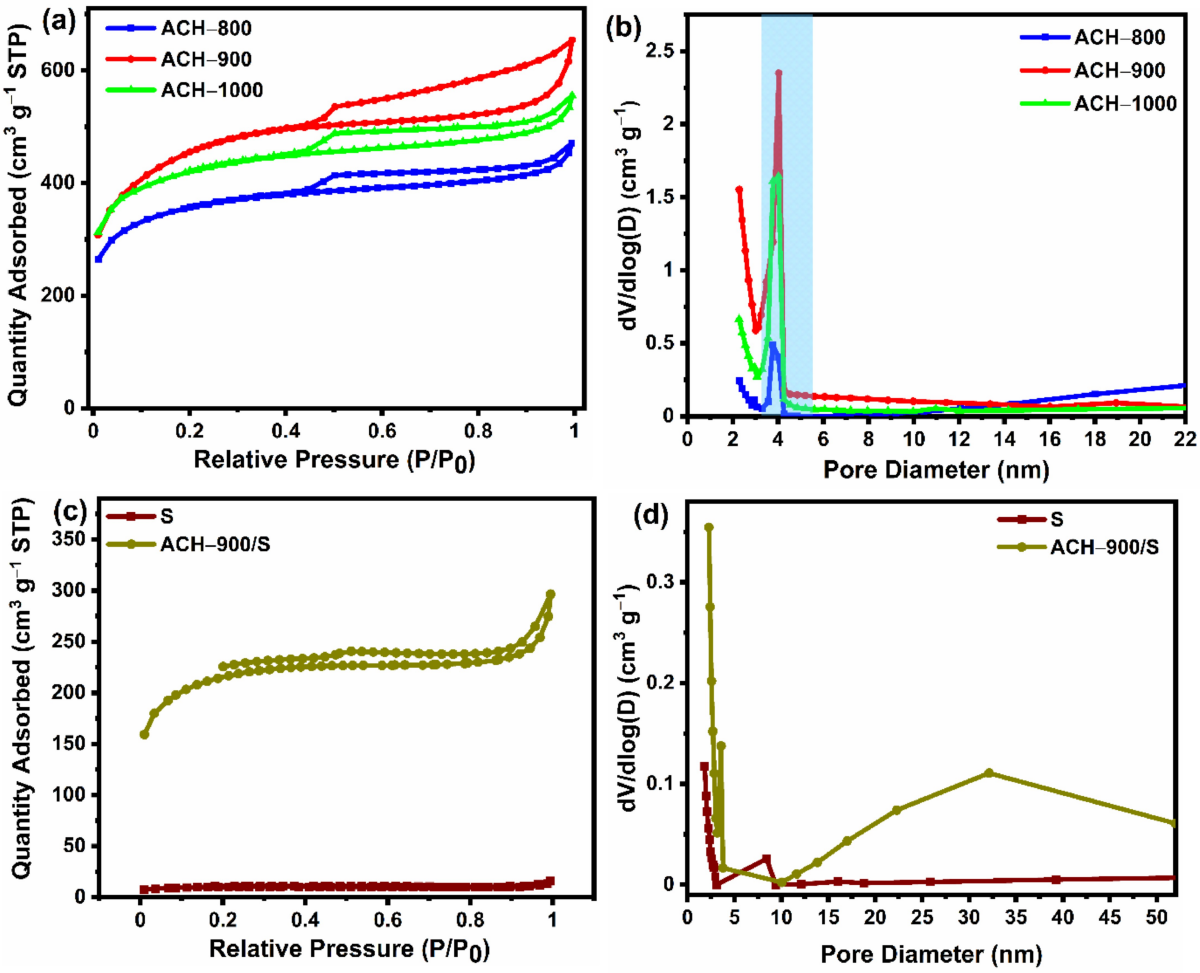

Figure 2. (a&b) N_2 adsorption/desorption isotherm and Pore size distribution (PSD) plot of ACH–T samples (c&d) N_2 adsorption/desorption isotherm and PSD plot of S, ACH–900/S samples.

[figure 2(d)] and larger pore size than that of ACH–900, mainly due to the growth of siloxene nanosheets in the pore of activated carbon (ACH–900) which reduces the total specific surface area to some extent. As depicted in Figure 2(b) and 2(d), calculated by the Barret-Joyner-Halenda (BJH) method, ACH–900 and ACH–900/S samples display average pore size of 2.82 nm and 3.25 nm, and the average pore volume calculated by single point method are 1.01 $cm^3 g^{-1}$ and 0.45 $cm^3 g^{-1}$ respectively. The smaller SSA, larger pore size and smaller pore volume of ACH–900/S further proves that the siloxene nanosheets are successfully grown and embedded in the pores of the ACH–900, and they still have pores of 692 $m^2 g^{-1}$, which provide favorable channels for electrolyte storage and ion transmission, further improving the capacitive properties of the composite.[45,46]

2.3. Raman Analysis

Figure 3(a) shows the Raman spectra of ACH–T samples recorded at an excitation wavelength of 532 nm. All the ACH–T samples spectra consist of two prominent peaks centered at 1335 ± 5 cm^{-1} and 1575 ± 5 cm^{-1} which correspond to D-peak for amorphous carbon and G-peak for sp^2 hybridized carbon atoms in graphitic phase, respectively.[8,47] Besides the D- and G-peaks, all the ACH–T samples present a second order 2D peak at a higher wave number of 2676 ± 5 cm^{-1} which indicates the presence of graphitized structures embedded inside the amorphous carbon framework.[38] The Raman spectra of ACH–T samples were deconvoluted using Voigt function [as shown in supporting information Figure S1 (a)-(c)] to obtain the integral areas of D1- and G-peaks which were used to calculate the disordered carbon (D) relative to the graphitic carbon (I_{D1}/I_G). Among the three samples, ACH–900 sample exhibits lowest I_{D1}/I_G (0.82) which reflects higher degree of graphitization or higher number of sp^2 hybridized graphitic carbons as compared to ACH–800 and ACH–1000 samples.

Figure 3(b) shows the Raman spectra of S, ACH–900, and ACH–900/S composite materials. Raman spectrum of the siloxene [Figure 3(b)] clearly depicts the Si–Si bands at 384 cm^{-1} and Si–O–Si band at 515 cm^{-1} respectively.[48,49] The low intensity peaks located at 644, 736 and 2115 cm^{-1} correspond to the presence of Si–H vibrations.[41,48] Furthermore, a low intensity broad peak at ~920 cm^{-1} was attributed to

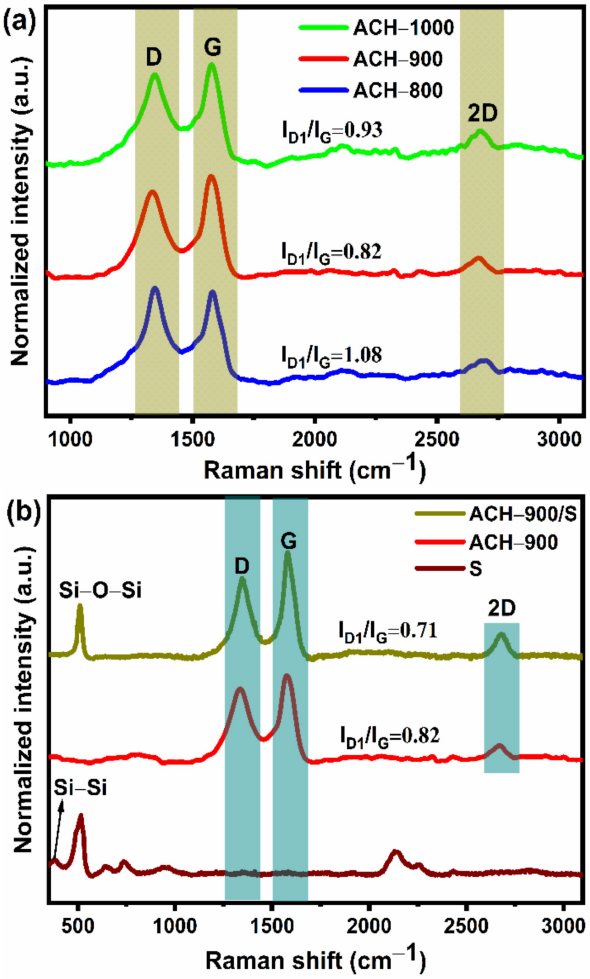

Figure 3. (a) Raman spectra of ACH–T samples (b) Raman spectra of S, ACH–900, ACH–900/S samples.

Si–OH vibration of siloxene.[50] The Raman spectrum of ACH–900/S composite presented in Figure 3 (b) indicates the successful formation of siloxene into the porous ACH–900 framework, based on the presence of one additional siloxene (Si–O–Si) peak at 515 cm^{-1} along with the typical amorphous carbon peaks at 1338 cm^{-1} (D-peak), 1576 cm^{-1} (G-peak) and 2681 cm^{-1} (2D-peak). The I_{D1}/I_G of ACH–900/S composite was calculated as 0.71 while the value was 0.82 for ACH–900, signifying the higher graphitization and lower amorphous carbon in ACH–900 after the introduction of siloxene (S). As mentioned earlier, the D and G bands of ACH–T and ACH–900/S samples are further deconvoluted into four separate bands as shown in supporting information Figure S1(a)–(d). These bands are centered around 1210 cm^{-1} (D4 band–polyenes/oligomers) 1336 cm^{-1} (D1 band–disordered/defective carbon structure), 1485 cm^{-1} (D3 band–amorphous carbon) and 1576 cm^{-1} (G band–graphitic carbon) respectively.

2.4. XPS Analysis

The high-resolution XPS measurements were performed to study the chemical bonding of the elements in $CaSi_2$, S, ACH–900, ACH–900/S samples and the corresponding survey spectra is shown in Figure 4 (a). The survey spectra of $CaSi_2$ shows the presence of major peaks assigned to Ca2p (347 eV), Si2p (101 eV), Si2 s (153.5 eV), C1s (284.5 eV), and O1s (532 eV) respectively.[8,12, 39] On the other hand, siloxene (S) sheets indicates the presence of Si2p (101 eV), C1s (284.5 eV), and O1s (532 eV) with trace amount of Ca on the surface of siloxene sheets which might relate to the residual Ca from the unreacted $CaSi_2$ based on the XRD [Figure 1 (a)].[12,14] The XPS spectra of ACH–900 and ACH–900/S sample reveals the presence of oxygen and carbon, with O1s, and C1s peaks at 532 eV, and 284.5 eV respectively whereas ACH–900/S composite shows a peak at 101 eV which corresponds to the presence of Si2p on the surface of activated carbon (ACH–900). Figure 4 (b) shows the Si2p spectra of the $CaSi_2$, S, ACH–900, ACH–900/S samples, where there is no significant variation in peak positions of Si2p peak of siloxene nanosheets. However, an increase in peak intensity corresponding to Si–Si (99.5 eV) and Si–O (102.6 eV) group for S and ACH–900/S samples in comparison to $CaSi_2$ samples corroborates the exfoliation of siloxene sheets and introduction of oxygen functionalities during calcium deintercalation process. To reveal the functional groups present in ACH–

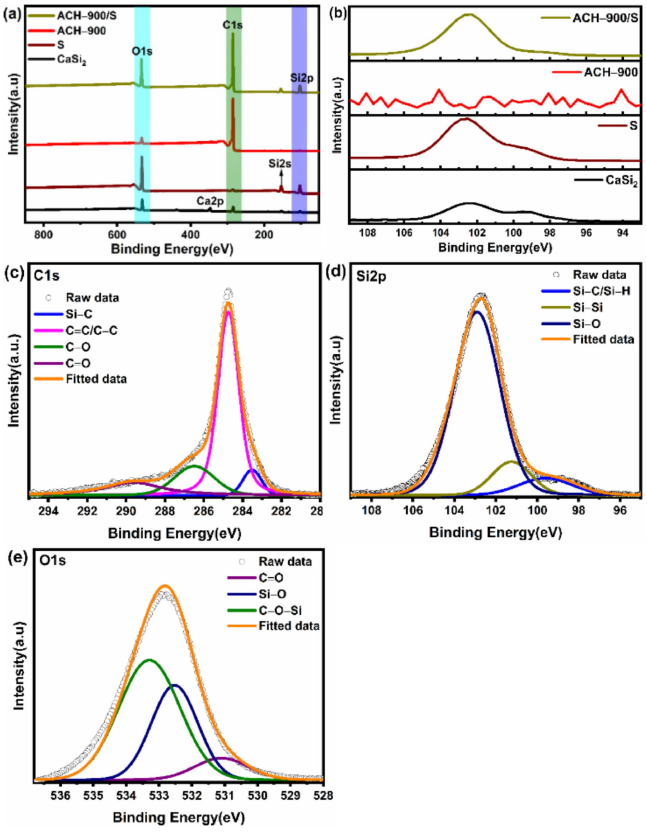

Figure 4. (a) XPS survey spectra for $CaSi_2$, S, ACH–900, ACH–900/S (b) Si 2p core level spectra from CaSi2, S, ACH–900, and ACH–900/S samples. (c) C1s, (d) O1s, and (e) Si2p core level spectra of ACH–900/S composite.

900/S, deconvolution of C1s, O1s and Si2p spectra of ACH–900/S composite was done and the results are displayed in Figure 4 (c & e). Deconvolution of C1s spectra [Figure 4 (c)] of ACH–900/S showed four peaks corresponding to Si–C (283.2 eV), C=C/C–C (284.5 eV), C–O (286.2 eV) and C=O (289 eV) respectively.[8,12] Si2p is deconvoluted into three peaks corresponding to the three types of silicon groups, Si–C/ Si–H (99.8 eV), Si–Si (101.2 eV), Si–O (102.9 eV), and Si–Si (104.2 eV) respectively.[12,51] As shown in Figure 4 (d), the O1s peak of ACH–900/S is deconvoluted into three peaks, corresponding to C=O (531 eV), Si–O (532.6 eV), C–O–Si (533.2 eV) groups.[14,48, 51] The peak at 533.2 eV for ACH–900/S further confirms the formation of C–O–Si bonds at the interfaces of activated carbon (ACH–900) and siloxene (S) sheets. In contrast to ACH–900 sample, ACH–900/S composite retained relatively high amount of oxygen which favors the enhancement of pseudocapacitance properties in the composite. The resulted activated carbon-siloxene (ACH–900/S) composite with increased oxygen-containing functional groups would improve the wettability and pseudocapacitance thus enhancing the overall energy storage performance.

2.5. FESEM Analysis

Field-emission scanning electron microscopy (FE-SEM) was used to analyse the surface morphology of the siloxene (S) sheets, ACH–900, and ACH–900/S composite, as illustrated in Figure 5. The sheet-like siloxene structures were visible in the FE-SEM images acquired at various magnifications on siloxane sample [Figure 5 (a–c)]. The densely packed siloxene structures restricts the movement of electrolyte ions thereby limiting the electro-

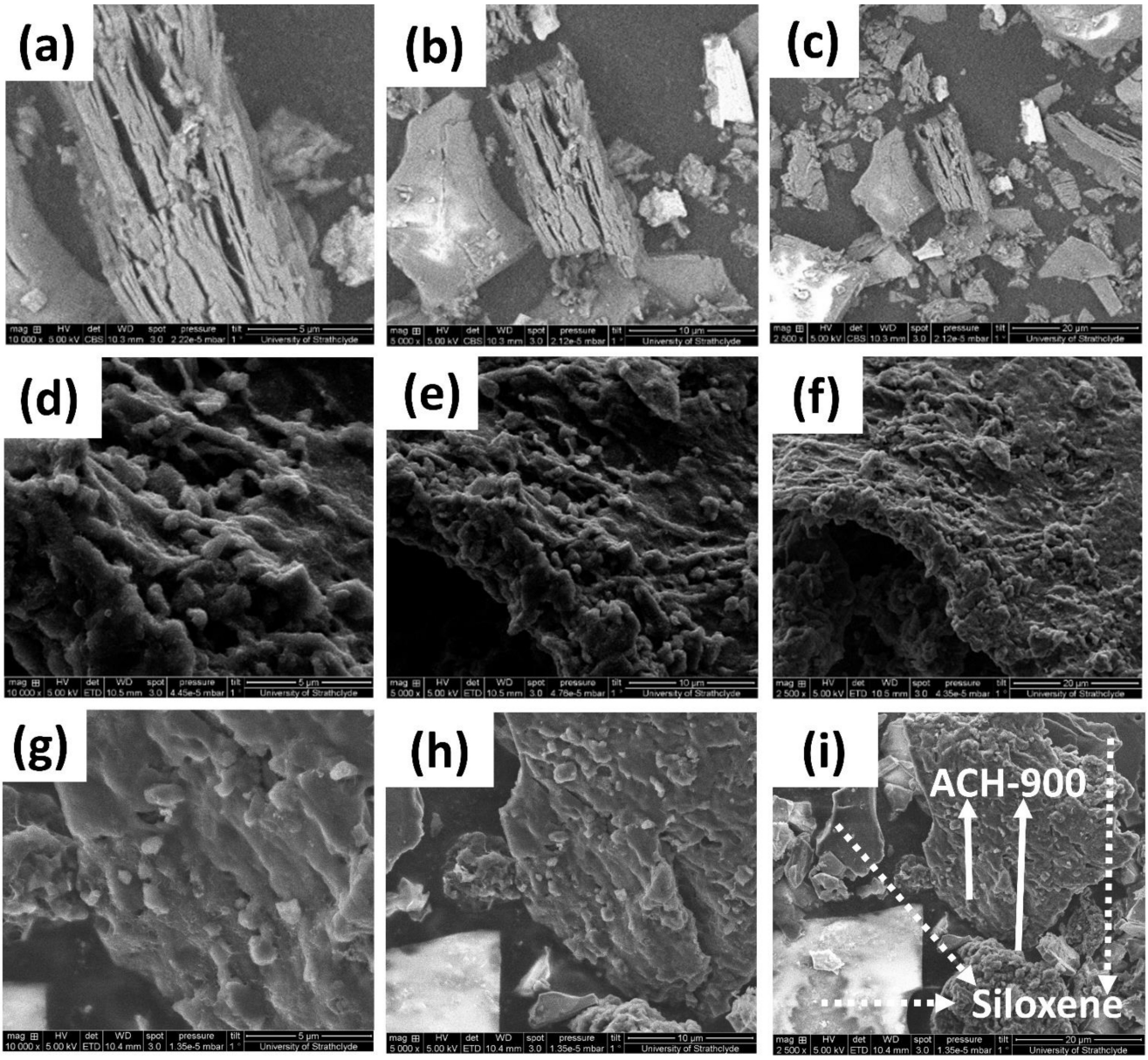

Figure 5. FESEM morphologies of (a-c) Siloxene (S) sheets (d-f) ACH–900 and (g-i) ACH–900/S composite at different magnifications.

chemical performance of siloxene (S) electrodes. The morphological features of ACH–900 sample shown in Figure 5 (d–f) shows the presence of rough and porous surface which might have resulted from the high temperature activation of the corn husk powder with $-KHCO_3$ as the pore-inducing activating agent. The rough and porous surfaced ACH–900 with high surface area (1508 $m^2 g^{-1}$) acts as an excellent support for hosting siloxene sheets. FESEM images of the ACH–900/S composite [figure 5 (g–i)] shows activated carbon (ACH–900) is deposited on the surface of the siloxene sheets. Due to the presence of functional groups on the surface of activated carbon matrix, the siloxene nanosheets tightly bond to the surface and inner pores of the porous carbon (ACH–900), which effectively reduces the stacking of siloxene sheets. Additionally, the siloxene sheets in the ACH–900/S composite help to speed up the interfacial transport of ions, and the narrow diffusion routes give the electrolyte ions more access during charging and discharging for better electrochemical performance. Furthermore, HAADF-STEM images of the ACH–900/S composite shown in Supporting Information Figure S2 (a) provided clear evidence of the coating of siloxene (S) on the porous ACH–900 framework. In addition, the elemental distribution also revealed the presence of C, O, and Si elements in ACH–900 composite as shown in Figure S2 (b–d).Benefiting from the synergistic effect of high surface porous carbon (ACH–900) and layered siloxene (S) structures, ACH–900/S composite electrode facilitates improved charge storage capability and reduces the ionic/electronic diffusion pathways making it an outstanding candidate for high-performance supercapacitor electrodes.

2.6. Electrochemical Analysis

2.6.1. Electrochemical Analysis of ACH–T Electrodes in 1 M Na_2SO_4 Electrolyte in Three Electrode Configuration

The electrochemical performance of the ACH–T electrodes was first measured in a three-electrode system in 1 M Na_2SO_4 electrolyte. The cyclic voltammograms (CV) of ACH–T electrodes acquired between −0.1 to 0.8 V was shown in Figure 6 (a, b) and Figure S3 (a, c) (Supporting Information). It can be seen that a scan rate of 5 $mV s^{-1}$, the CV curves of ACH–T electrodes exhibited a rectangular shape without any redox peaks, suggesting the charge storage is electrical double-layer capacitor (EDLC) behaviour. On the other hand, ACH–800 displayed a -smaller and distorted rectangular shaped CV curve suggesting lower charge storage capacity compared to ACH–900 and ACH–1000 electrodes. The CV curves [Figure 6 (a)] recorded at a sweep rate of 5 $mV s^{-1}$ further show that the ACH–900 exhibits the highest current density and larger rectangular loop area, indicating the highest specific capacitance. This can be explained by the fact that the SSA (1508 $m^2 g^{-1}$) and pore structure of the ACH–900 are higher, leading to an increase in the number of surface-active sites that the electrolyte ions can access, boosting the energy storage capacitance. The CV graphs of an ACH–900 and ACH–800, ACH–1000 working electrodes examined at various scan rates ranging from 5 to 100 $mV s^{-1}$ are shown in Figure 6 (b) and Figure S3 (a, c). Within the same potential window, it can be seen that the CV curves resemble rectangular shapes at lower scan rates (5–25 $mV s^{-1}$) and have a

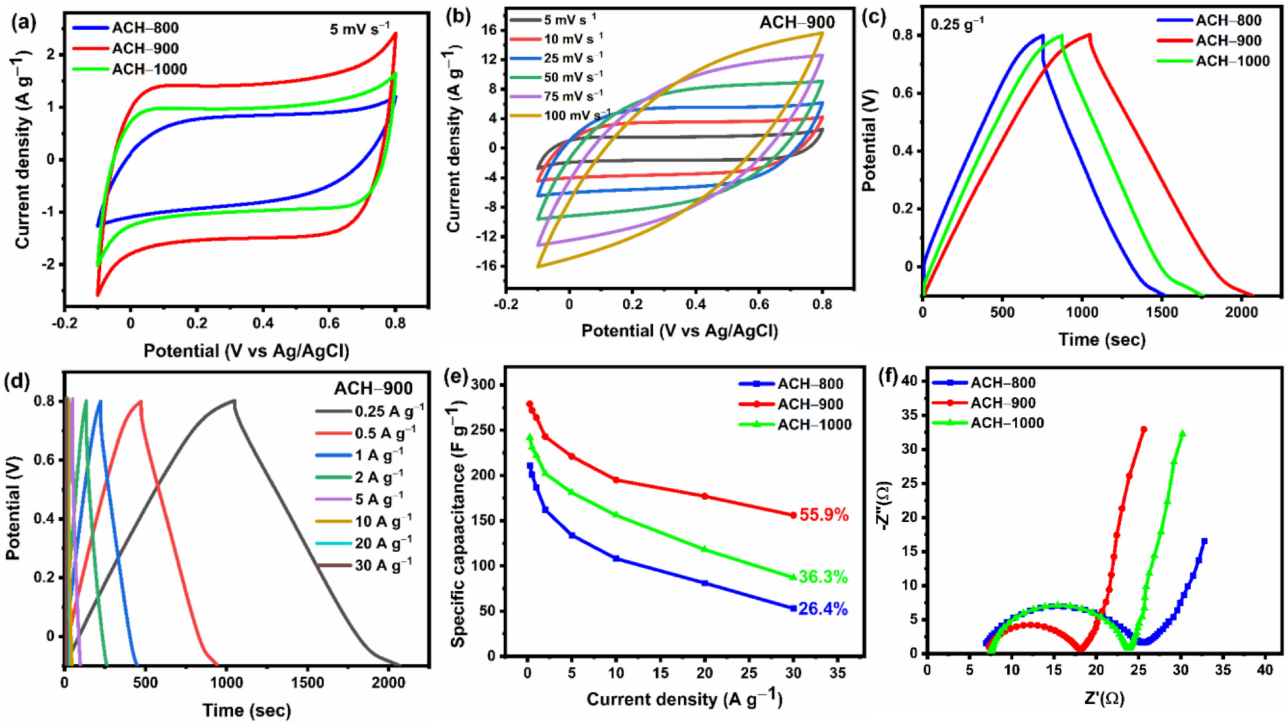

Figure 6. Electrochemical performance of the as-prepared ACH–T electrodes measured in a three-electrode system in 1M Na_2SO_4 electrolyte (a) Cycling voltammetry (CV) curves of ACH–T electrodes at a scan rate of 5 $mV s^{-1}$ (b) CV curves of ACH–900 electrode at different scan rates (c) GCD curves of ACH–T electrodes at a current density of 0.25 $A g^{-1}$ (d) GCD curves of ACH–900 electrode at different current densities (e) Specific capacitance of ACH–T electrodes plotted as a function of different current densities (f) Nyquist plots for all of the ACH–T electrodes.

quasi-rectangular shape at higher scan rates (50–100 mV s^{-1}). The reason for this quasi-rectangular shaped curve is because at higher scan rates, the electrolyte ion diffusion inside the pores of the electrode has a limited reaction time, resulting in a distortion of its double layer behaviour.[52] More specifically, the limited reaction time at higher scan rates prevents ionic movement inside the pores of electroactive material, leaving only the exterior surface of the material available for charge storage. In contrast, the electrolyte ions can access the entire surface area of the electrode material at lower scan rates resulting in a rectangular shaped CV curve.

The specific capacitance and rate capability of the ACH–T electrodes was examined from the galvanostatic charge discharge (GCD) measurements as shown in Figure 6(c,d) and Figure S3 (b, d) (Supporting Information). At 0.25 A g^{-1} current density, ACH–T electrodes display quasi-linear charge discharge curves indicating efficient ion transport and optimal electric double-layer capacitor behaviour. Additionally, the GCD curve of ACH–900 at 0.25 A g^{-1} exhibits a longer charge/discharge time than other samples [Figure 6(c)], suggesting that more electrolyte ions participate in the charge/discharge process in ACH–900, which leads to a larger specific capacitance. Figure 6(d) depicts the corresponding GCD graph of ACH–900 electrode at different current densities ranging from 0.25 to 30 A g^{-1}, where all curves are close to isosceles triangles, indicating that ACH–900 has excellent electrochemical reversibility and capacitive property even at higher current density. Based on the discharge curves, the specific capacitance values of ACH–T samples as a function of current density are calculated and the results are shown in Figure 6(e). ACH–900 exhibits a high specific capacitance of 279 F g^{-1} at current density of 0.25Ag^{-1}, which is much higher than ACH–800 (211 F g^{-1}) and ACH–1000 (242F g^{-1}). Interestingly, ACH–900 maintains a high specific capacitance of 156 F g^{-1} (~56% retention) even at an ultrahigh current density of 30 A g^{-1}, indicating excellent rate capability at high current densities than the other samples. The exceptional electrochemical performance of ACH–900 is a result of its high accessible surface area, which promotes charge storage, and its high degree of graphitization, which efficiently enhances electron/ion transport properties.

To further probe the charge transfer resistance and ionic diffusion properties at different activation temperatures, electrochemical impedance spectroscopy (EIS) was carried out and the corresponding Nyquist plot for ACH–T electrodes are shown in Figure 6(f). The impedance measurements were carried out within a frequency range of 0.01 mHz to 100 kHz with an AC perturbation of 5 mV. The Nyquist plot is a combination of nearly straight line in the low frequency region and a semicircle in high frequency region which is the characteristic of ideal electrochemical double layer behaviour. The intercept of the plot at the Z′ axis represented the equivalent series resistance (R_s) in the high frequency region, which is the sum of the internal resistance of the activated carbon materials, electrolyte resistance, and contact resistance between the electrode material and current collector.[8,53] The diameter of the semicircle in the high frequency region gives the charge transfer resistance (R_{ct}) of the electroactive material. In the presence of 1 M Na_2SO_4 electrolyte, the R_{ct} value is of the order of ACH–900 (10.7 Ω) > ACH–1000 (16.1 Ω) > ACH–800 (19.2 Ω). The decreased charge transfer resistance of ACH–900 shows that the electrode is more capacitive and possess most efficient and shortest charge transport pathways within the porous carbon framework. On the other hand, R_s values of the ACH–800, ACH–900 and ACH–1000 are in the order of 6.4, 7.1 Ω and 7.8 Ω respectively. The R_s of ACH–800 is the lowest among all the samples which might be due to the presence of high oxygen and nitrogen content in ACH–800 sample whose presence increases the surface wettability of the electroactive material with the current collector thereby reducing the contact resistance.[8,54] Based on the initial electrochemical data of ACH–T electrodes, the excellent behavior of ACH–900 can be summarized as follows: (1) The high SSA enabled sufficient surface active sites for charge adsorption/desorption thus resulting in high specific capacitance (2) The hierarchical porous structure with higher degree of graphitization provided abundant charge transport channels and shorter diffusion pathways, which are beneficial to improve rate performance and reduce charge transfer resistance. As ACH–900 material displayed high surface area, high degree of graphitization and excellent electrochemical performance compared to the other corn husk based activated carbons, it is employed as a template for the growing siloxene nanosheets inside the porous carbon network.

2.6.2. Electrochemical Analysis of S, ACH–900, ACH–900/S Electrodes in 1 M Na_2SO_4 Electrolyte in Three Electrode Configuration

According to the structural and morphological analysis, the ACH–900/S composite exhibited lowest graphitization degree, sufficient heteroatoms and hierarchical porous structure coated with siloxene sheets. Therefore, it is expected to have better electrolyte accessibility, high specific capacitance and high rate capability making them potential candidates for high-performance supercapacitor electrodes. The electrochemical performance of S, ACH–900, and ACH–900/S was tested in three-electrode test system with 1 M Na_2SO_4 and the corresponding results are showed in Figure 7. As can be seen from the Figure 7(a), the CV curves of S, ACH–900, and ACH–900/S at a scan rate of 5 mV s^{-1} display rectangular shape, indicating a double layer charge storage mechanism. The current response of siloxene (S) is very low with a small area rectangular curve, thus indicating very low specific capacitance. Compared to the pure S and ACH–900 electrode, ACH–900/S composite electrode displayed larger rectangular loop area, indicating that the introduction of siloxene sheets has a significant impact on the electrosorption performance of the composite. According to Figure 7(b) for the ACH–900/S composite electrode, the CV curve tends to be deformed from a normal rectangular shape into a leaf-like shape when the sweep speed rises from 5 to 100 mV s^{-1}. This behavior happens because the ions do not have sufficient time to access the interior of the electrode

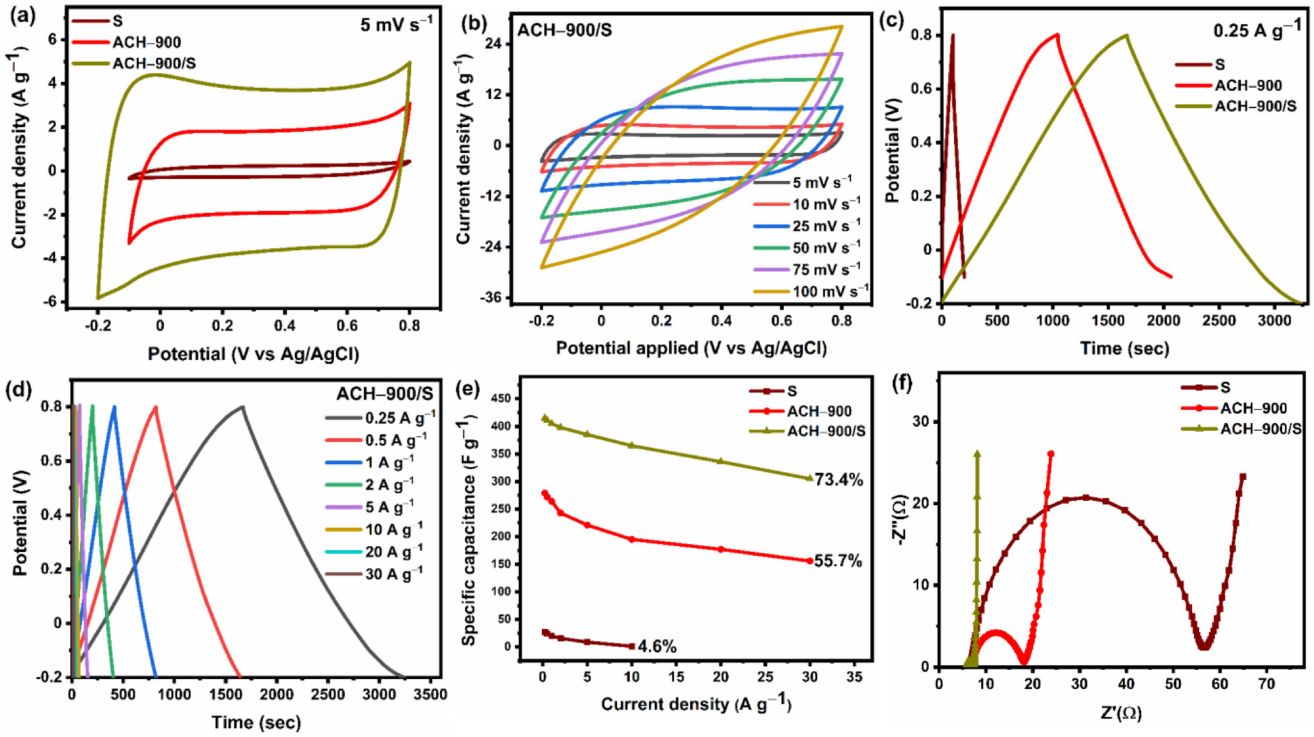

Figure 7. (a) Cycling voltammetry (CV) curves of S, ACH–900, ACH–900/S electrodes at a scan rate of 5 mV s^{-1} (b) CV curves of ACH–900/S electrode at different scan rates (c) GCD curves of S, ACH–900, ACH–900/S electrodes at a current density of 0.25 A g^{-1} (d) GCD curves of ACH–900/S electrode at different current densities (e) Specific capacitance of S, ACH–900, ACH–900/S electrodes plotted as a function of different current densities (f)) Nyquist plots for all of the S, ACH–900, ACH–900/S electrodes measured in a three-electrode system in 1M Na_2SO_4 electrolyte.

materials restricting the electrical double-layer formation at high scan rates.[55,56]

A further detailed study of the S, ACH–900, and ACH–900/S electrodes was conducted using charge-discharge experiments to assess the specific capacitance of all the electrodes at 0.25 A g^{-1} as shown in Figure 7(c). The charge-discharge profile presents a symmetrical triangle with a certain curvature, showing the synergistic effect of pseudocapacitance and double-layer capacitance, in agreement with the CV curves. The ACH–900/S electrode exhibited the longest discharge time indicating high specific capacitance which is in line with CV curves shown in Figure 7(a). The galvanostatic charge and discharge profiles of ACH–900/S was tested at various current densities (0.25–30 A g^{-1}) within −0.2 to 0.8 V voltage window as shown in Figure 7(d). It can be observed that the ACH–900/S composite electrode display nearly linear and triangular shaped charge-discharge curves even at higher current densities suggesting an excellent electrochemical reversibility and high rate capability. In order to compare the electrochemical performance of S, ACH–900, and ACH–900/S electrodes more intuitively, the specific capacitances are calculated from the discharge curves at different current densities from eq. (1). Figure 7(e) shows the specific capacitance plotted as a function of current density for all the electrodes. As shown in Figure 7(e), the capacitance of the S, ACH–900, and ACH–900/S electrodes at 0.25 A g^{-1} are 27 F g^{-1}, 279 F g^{-1}, and 415 F g^{-1}, respectively. Furthermore, ACH–900/S composite electrode with a high capacitance of 415 F g^{-1} at a current density of 0.25 A g^{-1} still shows 73.4% (305 F g^{-1}) capacitance retention at a current density of 30 A g^{-1}. As the current density continues to increase, the ability to move and get close to the inside of the electrode surface is suppressed. In other words, excessive current density might harm the effective surface of the electrode, resulting in a decrease in specific capacitance. The specific capacitance value of the ACH–900/S composite electrode is greater than the sum of that of a pure S and ACH–900 electrodes and its outstanding rate performance can be attributed to its distinctive porous structure which is a combination of high surface area activated carbon and 2D siloxene sheets. We believe that ACH–900 supports the siloxene sheets to construct a highly open porous matrix, which provides good connection and greatly reduces the ionic transport pathways. Moreover, hierarchical porous structure of ACH–900/S provides stable and efficient channels for the transmission of ions/electrons in the electrode, which also significantly increases the capacitance and rate performance. Table 1 clearly shows the performance of ACH–900/S composite electrode studied in this work is comparable and even better than some of corn based activated carbon electrodes and also activated carbon/2D material composites reported in the literature. From the above results, we conclude that the ACH–900/S electrode achieved excellent electrochemical performance with high specific capacitance, excellent rate capability, better conductivity with lower series and charge transfer resistance in 1 M Na_2SO_4 aqueous electrolyte.

Electrochemical impedance spectroscopy tests were carried out on S, ACH–900, and ACH–900/S electrodes within a

Table 1. Comparison of electrochemical performance (specific capacitance) of ACH–900/S composite electrode with other corn based activated carbon electrodes and also activated carbon/2D material composites reported in the literature.

Electrode material	SSA ($m^2\ g^{-1}$)	Electrolyte	Specific Capacitance ($F\ g^{-1}$)	Ref.
AC 0.9 (Corn cob)	1288.0	1 M H_2SO_4	340.8 at 5 $mV\ s^{-1}$	57
CS–AKAC (Corn straw)	1067.1	6 M KOH	239 at 1 $A\ g^{-1}$	58
NCSAC (Corn stalk)	2152	6 M KOH	350.4 at 0.2 $A\ g^{-1}$	59
CH–650–2 (Corn husk)	1115	0.5 M H_2SO_4	269 at 5 $mV\ s^{-1}$	60
ACS–700 (corn Cob)	254	1 M Na_2SO_4	159 at 0.25 $A\ g^{-1}$	61
CHAC (Corn husk)	1109	25% SW (sea water)	149 at 1 $A\ g^{-1}$	62
ACH 600 (Corn husk)	771	0.5 M H_2SO_4	297.81 $F\ g^{-1}$ at 5 $mA\ cm^{-2}$	63
ACH–900	1508	1 M Na_2SO_4	279 at 1 $A\ g^{-1}$	This work
MG@AC–3	1174.4	3 M H_2SO_4	442 at 2 $mV\ s^{-1}$	9
CPCM/MXene (Chitosan)	1649	1 M H_2SO_4	364 at 0.5 $A\ g^{-1}$	11
Siloxene/RGO	–	1 M H_2SO_4	520 at 1 $A\ g^{-1}$	13
GOAC–3 (Chitosan)	1257.6	1 M H_2SO_4	375.7 at 1 $A\ g^{-1}$	64
ACH–900/S	692	1 M Na_2SO_4	415 at 1 $A\ g^{-1}$	This work

10 mHz–100 kHz at 5 mV amplitude in order to understand the electro transport kinetics of the as-prepared electrodes. As shown in Figure 7(f), Nyquist plot of all the samples presented two distinctive features, a semicircle in the high frequency region followed by a steeper line in low frequency region. With the addition of siloxene sheets onto the activated carbon, the semicircle loop diameter gradually decreased and showed an approximately vertical line at low frequency. The equivalent series resistance (R_s) and the charge transfer resistance (R_{ct}) are calculated from the intercept at real axis and the semicircle intercepts in the high frequency region (after equivalent circuit fitting) of the Nyquist plot.[65] In the high-frequency region, the ACH–900/S shows an equivalent series resistance of 5.8 Ω which is smaller than the pure ACH–900 (7.3 Ω) and S (6.8 Ω) electrodes. The lower R_s of ACH–900/S electrode can be attributed to the increased oxygen contained functional groups generated from the addition of siloxene sheets onto porous carbon matrix. It is believed that these oxygen containing functional groups can boost wettability of the electrodes thereby enhancing the adhesion between electroactive material and the current collector.[11,13] Meanwhile, R_{ct} originates from the electrolyte ion transfer across the entire interface of electrode materials in contact with the electrolyte solution. The R_{ct} for the siloxene (S) sheets is 48.6 Ω suggesting the S electrode has a relatively low electrical conductivity and small electroactive surface area (evident from BET plots shown in Figure 2(c)). However, when siloxene sheets are decorated on the ACH–900, the R_{ct} for ACH–900/S composite electrode was measured to be 1.4 Ω which is lower than that of ACH–900 (10.7 Ω) which means that the composite electrode possesses better charge transport kinetics than the pure activated carbon. We believe that the addition of siloxene sheets creates more channels for the rapid diffusion of electrolyte ions inside the porous framework, whereas ACH–900 avoids the stacking of siloxene layers, shortening the diffusion path of electrolyte ions and reducing the R_{ct}. Moreover, the steep line of ACH–900/S is more perpendicular than ACH–900 and S electrodes in low frequency region indicating that the former has a more ideal capacitance behavior. To further understand the electrochemical properties of ACH–900/S electrode, we fitted the impedance spectra of the composite electrode and the corresponding equivalent circuit model was shown in the Supporting Information (Figure S4(e)). The equivalent circuit consist of a combination of the following components: R_s, R_{ct}, constant phase element (CPE), and double-layer capacitance (C_{dl}). The R_{ct}-C_{dl} circuit is responsible for ion transfer within the composite electrode framework at high-mid frequencies. The nearly straight line in the low-frequency area of the Nyquist plot reveals the capacitive behavior of corn-based activated carbon electrodes, represented by CPE. These results show that the addition of siloxene sheets to the porous carbon framework can effectively enhance the transport of electrons/ions thereby promoting the conductivity and electrochemical performance of ACH–900/S composite electrode.

2.6.3. Symmetric Supercapacitor Study in two Electrode Configuration

To further probe into the advantages of the ACH–900/S composite material in practical applications, a symmetric Swagelok cell supercapacitor was assembled with ACH–900/S composite as electrode and highly concentrated 8 m $NaClO_4$ AWIS as electrolyte. According to eq. (4), the cell voltage (ΔV) has a significant impact on the ability of supercapacitor to store energy because its energy density (E_d) is directly proportional to the square of the voltage. So, in our investigation, we first looked into the impact of voltage window on the electrochemical performance of the supercapacitor by using cyclic voltammetry (CV) at a constant scan rate of 5 $mV\ s^{-1}$. As shown in Figure 8(a), the quasi rectangular shape of the CV curves is persistent up to 3.0 V, revealing the reversible adsorption/desorption of ions on the electrode surface. Further increasing

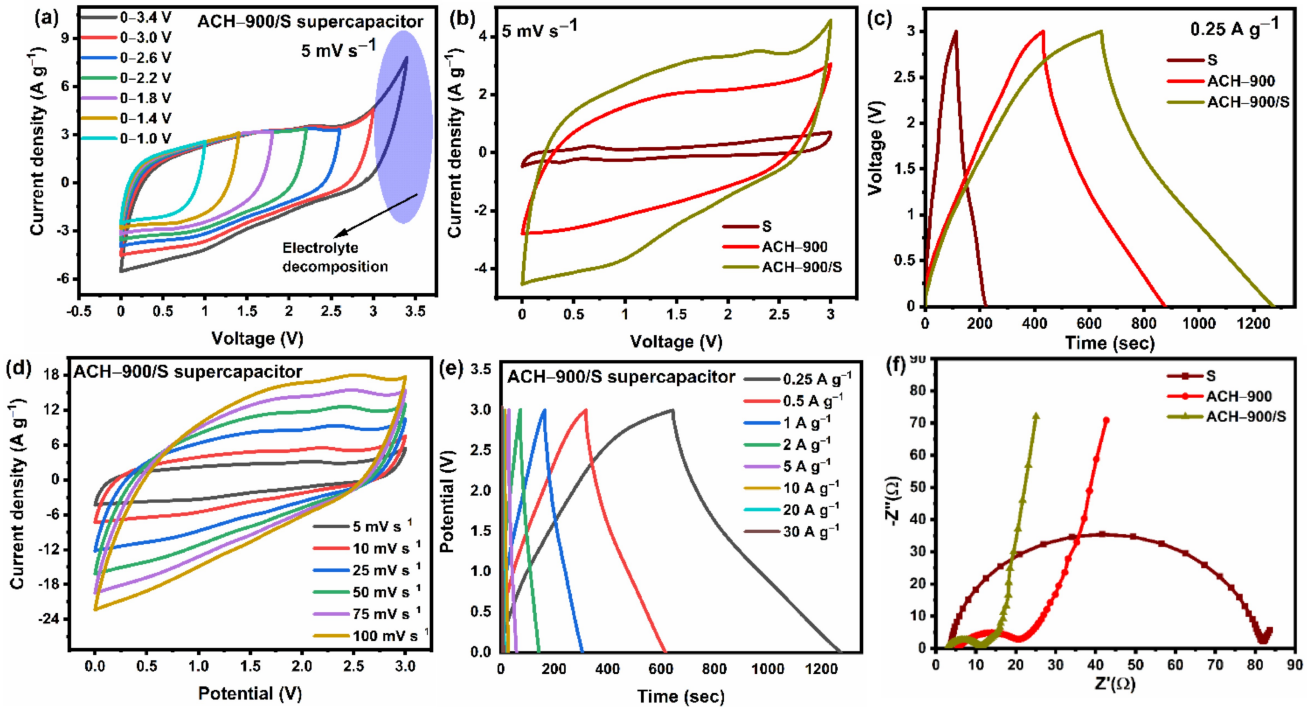

Figure 8. (a) CV curves of the symmetric supercapacitor based on ACH–900/S using $NaClO_4$ based acetonitrile water-in-salt (AWIS) electrolyte measured at different voltage windows at 5 mV s^{-1} scan rate (b) Cyclic voltammograms of S, ACH–900, ACH–900/S electrodes based supercapacitor recorded using a scan rate of 5 mV s^{-1} over a voltage window of 3.0 V (c) Charge-discharge profiles of S, ACH–900, ACH–900/S electrodes based supercapacitors recorded at a current density of 0.25 A g^{-1} over a voltage window of 3.0 V (d) CV curves of the ACH–900/S supercapacitor using $NaClO_4$ based acetonitrile water-in-salt electrolyte at different scan rates (5–100 mV s^{-1}) (e) GCD curves of the ACH–900/S supercapacitor at various current densities (0.25–30 A g^{-1}) (f) Nyquist plots of S, ACH–900, ACH–900/S electrodes based supercapacitors recorded using 8 m $NaClO_4$ AWIS electrolyte.

the upper cut-off potential to 3.4 V completely ruins the supercapacitor performance by a steep increase in the current response, which eventually accelerates the electrolyte decomposition. Hence, the upper cut-off potential is fixed to 3.0 V for further studies. The cyclic voltammograms of the S, ACH–900, ACH–900/S supercapacitors recorded over an operational potential window of 0–3.0 V at a scan rate of 5 mV s^{-1} are shown in Figure 8(b). The area of the cyclic voltammogram is higher for the ACH–900/S electrode based symmetric supercapacitor than for bare siloxene and ACH–900 supercapacitors, thus highlighting its enhanced charge-storage properties. In addition, redox peaks can be seen in the CV curves of the S and ACH–900/S electrode-based supercapacitor, showing a mix of double layer and pseudocapacitive behaviour. The pseudocapacitive behavior might be attributed to redox reactions of electrochemically active oxygen-containing functional groups on the electrode material surface which is evident from the XPS survey spectra shown in Figure 4(a). We used galvanostatic charge discharge analysis, which is an appropriate method to evaluate a series of supercapacitor performance metrics. The GCD profiles shown in Figure 8(c) represent a distinctive symmetric shape with small plateaus at the end of charging and discharging curves, demonstrating the little influence of pseudocapacitance. The charge discharge profiles of the fabricated supercapacitors recorded at an applied current density of 0.25 A g^{-1} reveal that the amount of charge storage is in the order of S < ACH–900 < ACH–900/S supercapacitor. The ACH–900/S electrodes supercapacitor possessed the highest specific capacitance of 204 F g^{-1}, which is higher than that of the ACH–900 supercapacitor (154 F g^{-1}), and siloxene (S) supercapacitor (40 F g^{-1}) recorded at an applied current of 0.25 A g^{-1}. Figure S6 (a), Figure S6(c) [Supporting Information], and Figure 8(d) represent the cyclic voltammograms of the bare siloxene, bare ACH–900, and ACH–900/S electrode based symmetric supercapacitor recorded using different scan rates. Typical quasi rectangular-shaped cyclic voltammograms were observed for all supercapacitors, and there were noticeable differences in the current density ranges. An increase in the current response as a result of an increase in the scan rates [Figure 8(d)] highlights the improved capacitive nature of the ACH–900/S supercapacitor. Figure 8(e), Figure S6 (b), Figure S6 (d) [Supporting Information], shows the charge discharge profiles of ACH-900/S, ACH-900, and S, supercapacitors. The GCD profiles showed nearly symmetric triangular shape of capacitive behavior under different current densities, revealing the high rate capability of ACH–900/S supercapacitor which agrees with CV graphs shown in Figure 8(d). For the ACH–900/S electrodes-based supercapacitor, specific capacitance of 204 F g^{-1} was achieved at low current density of 0.25 A g^{-1} and still maintained 38.7% (79 F g^{-1}) of its initial capacitance even at a high current density 30 A g^{-1} further demonstrating the good rate capability.

Figure 8(f) shows the Nyquist plots of S, ACH–900, ACH–900/S electrodes-based supercapacitor in the scanning fre-

quency range of 10 mHz–100 kHz and amplitude of 5 mV. The equivalent series resistance (R_s) and charge transfer resistance (R_{ct}) of the sample are obtained from the EIS curve fitting. The R_s values of S, ACH–900, ACH–900/S electrodes-based supercapacitor are 3.5, 5.5, and 2.8 Ω, respectively. The decreased R_s of the ACH900/S supercapacitor can be due to the increased oxygen containing functional groups which improve the electrode wettability, hence improving adhesion between electroactive material and current collector. The R_{ct} values of S, ACH–900, ACH–900/S electrodes-based supercapacitor are 77.8, 16.6, and 8.6 Ω, respectively. The ACH–900/S electrodes-based supercapacitor has lowest R_{ct} (8.6 Ω) and R_s (2.8 Ω), which signifies that the efficient electron and ion transport inside the porous activated carbon framework which is enabled by the presence of siloxene sheets. The Nyquist plot of ACH–900/S electrodes-based symmetric supercapacitor was analyzed using equivalent circuit model as shown in Figure S6(e) [Supporting Information]. The x-intercept in the high frequency area reflects the equivalent series resistance (R_s), which is a sum of the electrolyte resistance, internal resistance of the active materials and substrate, and contact resistance with the collector.[8] At high-mid frequency region, the semicircle is represented by the parallel combination of charge transfer resistance (R_{ct}) [related to the electrochemical reactions at the interfaces of active materials] and constant phase element (CPE) [indicating the non-ideal capacitive behavior of the double layer].[66] The semi-infinite linear diffusion and transport of electrolyte to and from the electrode plane as well as in the porous electrode is represented by the Warburg impedance (W), which is the cause of the sloped line (45°) at low frequencies. Behind the W line, a nearly straight line is the formation of double layer (C_{dl}) which indicates the stored charges on the electrode/electrolyte interfaces which is proportional to the electroactive surface area.[67,68]

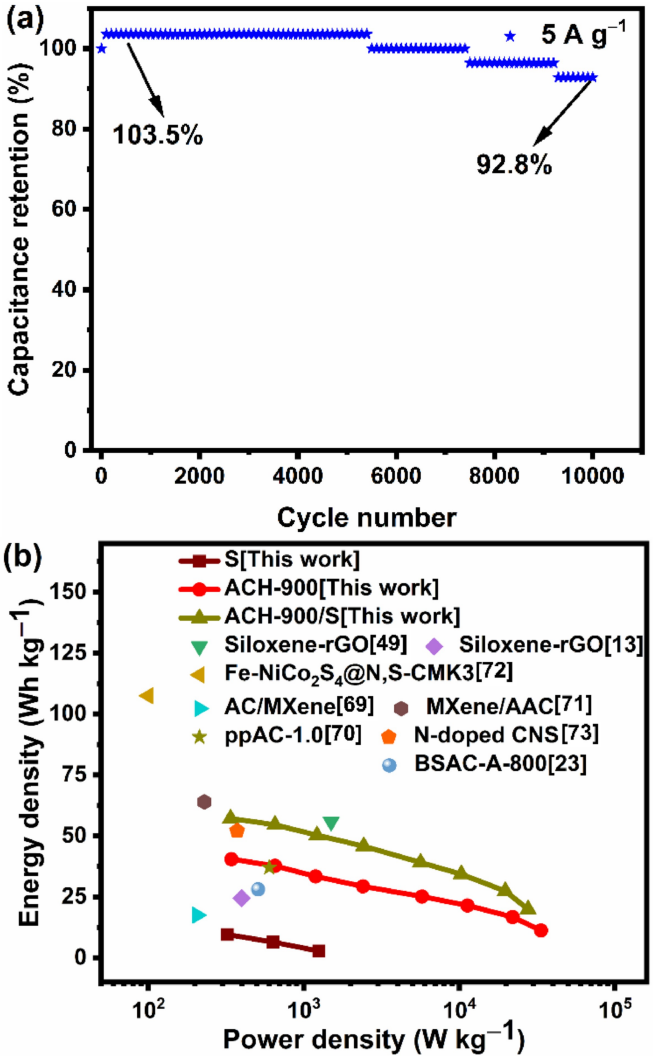

Figure 9. (a) Long-term cyclic stability of ACH–900/S electrodes-based supercapacitor carried over 10000 charge/discharge cycles at 5 A g^{-1} current density (b) Ragone plot of ACH–900/S electrodes-based supercapacitor indicating their energy–power performance metrics that are superior to those reported in the literature.

2.6.3.1. GCD Tests for 10000 Cycles and Ragone Plot for ACH–900/S Symmetric Supercapacitor

Figure 9(a) shows the cyclic stability graph of the device measured for 10000 charge/discharge cycles at 5 A g^{-1} current density in 8 m $NaClO_4$ AWIS electrolyte. The long-term stability tests over 10000 cycles showed that the ACH–900/S composite supercapacitor retained 92.8% of its initial capacitance even after 10000 charge/discharge cycles. The electroactivation effect i.e., complete activation of electrode surface during the continuous charge/discharge process was observed in the long-term stability performance of the ACH–900/S composite supercapacitor where the capacitance increased to 103.5% (5200 cycles), followed by a gradual decay up to 92.8% (10000 cycles), thus suggesting their excellent long-term stability. The decrease in capacitance might be due to the stacking of the siloxene nanosheets and graphitic carbon, which leads to less penetration of electrolyte ions into the pores of the electrolyte.

The Ragone plots of S, ACH–900, ACH–900/S electrodes-based supercapacitor for energy density (E_d, W h kg^{-1}) and power density (P_d, W kg^{-1}) in 0 to 3.0 V potential window are examined in Figure 9(b). Owing to its high specific capacitance and wide operational voltage window, the ACH–900/S electrodes-based supercapacitor exhibited a remarkable energy density of 57.2 W h kg^{-1}, which is considerably larger than that of the siloxene (S) electrodes-based supercapacitor (9.56 W h kg^{-1}) and ACH–900 electrodes-based supercapacitor (40.5 W h kg^{-1}) at a corresponding current density of 0.25 A g^{-1}. As shown in Figure 9(b), the energy density of the ACH–900/S supercapacitor varied from 57.2 to 19.6 W h kg^{-1}, with an increase in the power density from 338 W kg^{-1} to 27.6 kW kg^{-1}, respectively. Figure 9(b) highlights that the performance of the ACH–900/S supercapacitor are comparable or superior to those of reported state-of-the-art symmetric supercapacitors based on Siloxene composites, Activated carbon/2D material composites and also the biomass activated carbon with Water-in-Salt and ionic liquid electrolytes.[13,23,49,69–73] For example, Pang et al.[23] reported the fabrication of symmetric supercapacitor with high surface area

(1037.6 $m^2 g^{-1}$) ground grain hull derived activated carbon and 17 m $NaClO_4$ WIS electrolyte which delivered an energy density of 47.2 $W h kg^{-1}$ within 2.4 V potential window. Similarly, Li et al.[73] reported symmetric supercapacitor with high surface area (2278.2 $m^2 g^{-1}$) gelatin derived activated carbon and non-flammable TEP/ $EMIMBF_4$ [triethyl phosphate (TEP)-1-butyl-3-methylimidazolium tetrafluoroborate] based organic electrolyte which exhibited an energy density of 52.1 $W h kg^{-1}$. In both these cases, it can be observed that the energy density values are lower when compared to the present work. The presence of siloxene sheets inside the porous ACH–900 offers additional and faster diffusion paths for electrolyte ions during rapid charge/ discharge processes and increase the accessibility of porous framework to electrolyte ions, leading to an improved rate capability and electrochemical performance than compared to the aforementioned works. From the Ragone plot, it can also be observed that the ACH–900/S composite based supercapacitor with AWIS electrolyte is comparable or better than the 2D materials/activated carbon devices reported by Yu et al.[69] and Li et al.[71] employing an aqueous electrolytes. Although the MXene/AAC composite supercapacitor reported by Li et al.[71] showed higher energy density in 6 M KOH electrolyte, the working voltage (1 V) of the as-prepared supercapacitor is lower limiting its use in practical application. Furthermore, as shown in Figure 9(b), ACH–900/S composite supercapacitor showed higher electrochemical performance compared to the other siloxene/rGO composite supercapacitors fabricated using 1.0 m $TEABF_4$ in acetonitrile and 1 M H_2SO_4 electrolytes reported in the literature.[13,49] We believe the use of the hybrid AWIS electrolyte enabled a safe 3.0 V supercapacitor that exhibited excellent electrochemical performance (specific capacitance, rate capability) in comparison to the supercapacitors using aqueous and even organic electrolytes.

2.6.3.2. Effect of Temperature on Electrochemical Performance of the ACH–900/S Electrodes-Based Supercapacitor with AWIS Electrolyte

The temperature dependent supercapacitive performance of ACH–900/S composite supercapacitor was conducted over a wide temperature range from 0 °C to 100 °C as shown in Figure 10. The cyclic voltammograms of the ACH–900/S composite supercapacitor displayed quasi-rectangular-shaped profiles at different temperatures. As the temperature gradually increases from room temperature (26 °C) to 100 °C, the current density as well as the integrated CV loop area for the device increased. The effect of temperature on the capacitive performance of the ACH–900/S electrode supercapacitor was calculated using the GCD graph shown in Figure 10(b). The specific capacitance at different temperatures revealed that with a rise in temperature from 0 °C to 100 °C, the capacitance of the ACH–900/S electrode supercapacitor increased from 182 $F g^{-1}$ to 242 $F g^{-1}$ at 0.5 $A g^{-1}$ current density. The device capacitance at 100 °C reaches 117% of that at room temperature (206 $F g^{-1}$) because of increased ionic conductivity and accelerated transfer

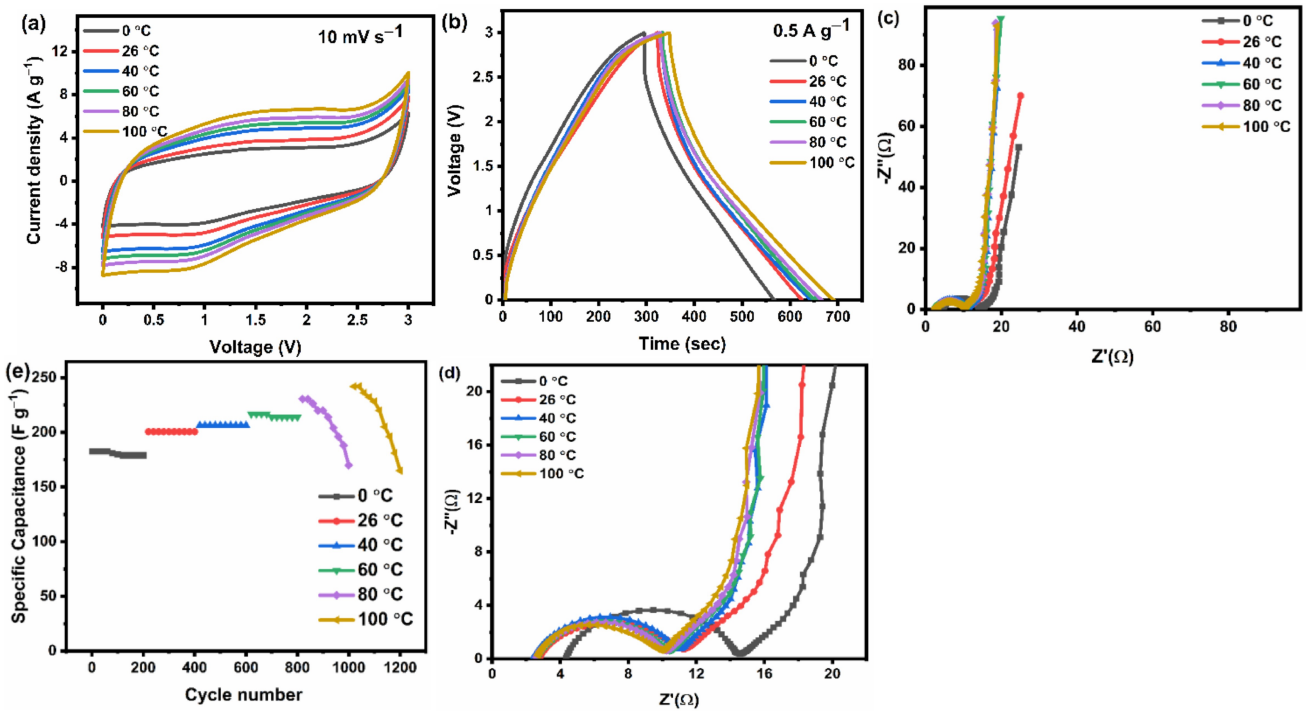

Figure 10. Temperature dependent performance of ACH–900/S electrode based Swagelok type supercapacitor in 8 m $NaClO_4$ AWIS electrolyte (a) CV curves of ACH–900/S electrode based supercapacitor recorded at a scan rate of 10 $mV s^{-1}$ (b) GCD curves of ACH–900/S electrode supercapacitor recorded at a current density of 0.5 $A g^{-1}$ (c) Nyquist curves of ACH–900/S electrode supercapacitor (d) Magnified image of Nyquist curves of ACH–900/S electrode supercapacitor over a wide temperature range from 0 to 100 °C (e) Specific capacitance measured at different temperatures at different temperatures 0 to 100 °C for 200 charge/discharge cycles at each temperature.

of ions from the electrolyte to electrode. Temperature-dependent electrochemical impedance spectroscopy (EIS) measurements was performed on the ACH–900/S electrode supercapacitor using 8 m $NaClO_4$ AWIS electrolyte and the corresponding Nyquist plot was shown in Figure 10(c). Under varied operating temperatures, all of the Nyquist plots displays the usual impedance behavior of typical supercapacitor, with a semicircle at high frequency region and a near vertical line at low frequency region. As shown in Figure 10(d), the semicircle at high frequency reflects the charge transfer resistance (R_{ct}), which demonstrates that the R_{ct} value reduces with the increase in temperature. This might be due to the enhanced mobility of electrolyte ions inside the pores of the composite electrode at high temperature. Notably, the capacitive line moves closer to the imaginary axis of the impedance as a result of the temperature change from 0 °C to 100 °C, indicating an increased capacitive nature for the ACH–900/S composite supercapacitor at elevated temperatures. With the increased temperature, the shifts of capacitive straight line along the real axis display decreased resistive values because the penetration of ions inside the pores becomes easier at higher temperature. Besides, the device cycling performance across 200 cycles at 0 °C to 100 °C showed a stable capacitance retention up until 60 °C as shown in Figure 10(e). But the capacitance started to decrease at higher temperatures of 80 °C and 100 °C which might be due to the rapid evaporation of solvent and also precipitation of salt. These results suggest that the ACH–900/S electrodes-based supercapacitor with AWIS electrolyte showed good temperature tolerance and cyclic stability indicating the applicability of ACH–900/S composite supercapacitor over a wide temperature range.

2.6.3.3. Practical Demonstration of the ACH–900/S Electrode-Based Swagelok Type Supercapacitor in 8 m $NaClO_4$ AWIS Electrolyte

To further demonstrate the performance of the fabricated supercapacitors in real-world applications, we tested the as-prepared supercapacitor by connecting to LED and DC fan. The device was initially charged to 3.0 V for 60 sec and discharged using LED's and DC fan. Here, the device performance was tested with LEDs of different voltage ranges: Red (1.6–1.8 V), Green (2.1–2.5 V), and Blue (3.0–3.6 V). The as-prepared supercapacitor with ACH–900/S electrode and 8 m $NaClO_4$ AWIS electrolyte efficiently powered red LED (652 sec), green LED (292 sec), blue LED (82 sec), and DC fan (261 sec), as shown in Figure 11(a–d). Because green and blue LEDs require high voltage, the supercapacitor can only power them for a shorter period of time than compared to red LED and DC motor.

3. Conclusions

The current work demonstrates the remarkable improvement in supercapacitor performance achieved by using 2D siloxene sheets in electrodes made from waste corn husk derived activated carbons (ACH–900). The siloxene sheets are supported by ACH–900 to create a porous network, which hinders the self-stacking and aggregation of the siloxene sheets and enhances the diffusion and transfer of electrolyte ions. The presence of siloxene sheets inside the porous ACH–900 framework reduces the ion diffusion paths, allowing for efficient and quick electron transport during the charge/discharge process and ensuring

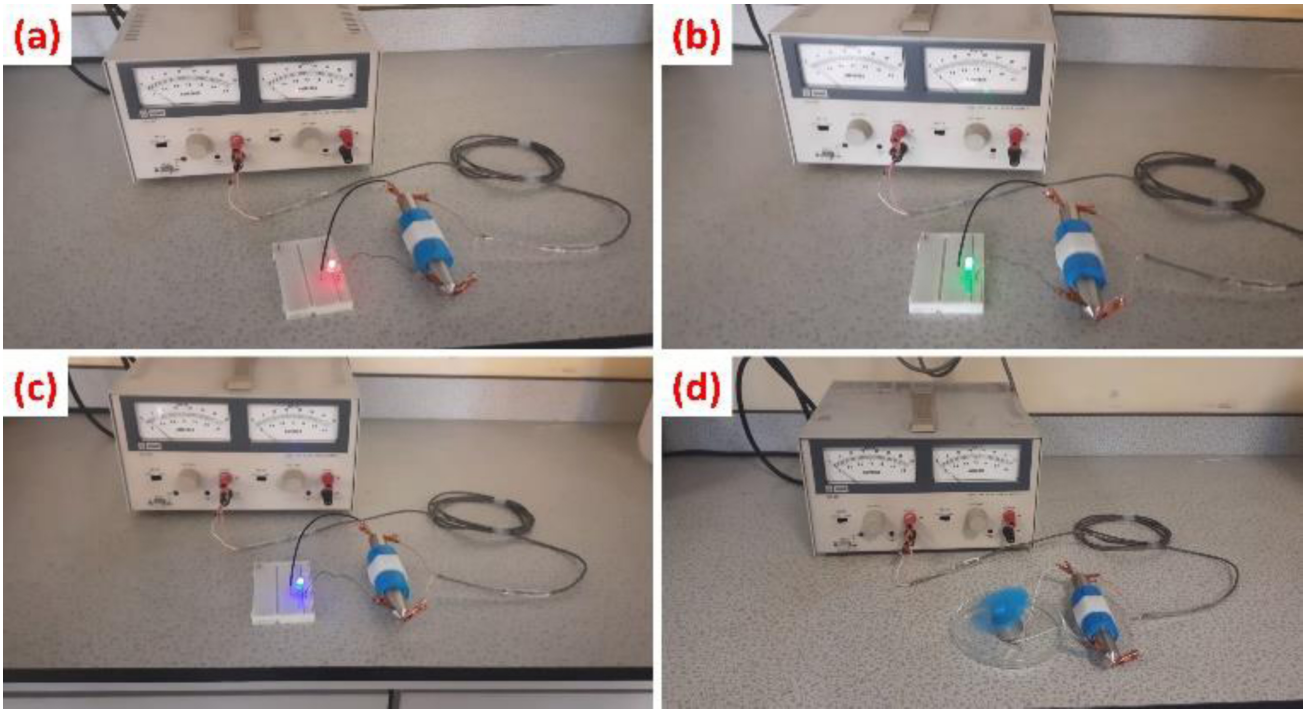

Figure 11. (a–d) Photographs of various LED's and DC fan powered by single Swagelok cell supercapacitor with ACH–900/S electrode and 8 m $NaClO_4$ AWIS electrolyte.

high specific capacitance of the composite electrode. When the ACH–900/S composite is tested as an electrode in three electrode system in 1 M Na_2SO_4 electrolyte, the electrode exhibited highest capacitance of 415 $F g^{-1}$ at 0.25 $A g^{-1}$ and retained 73.4% of its initial capacitance even at higher current densities (0.25 $A g^{-1}$). Moreover, the as-prepared symmetric supercapacitor with ACH–900/S composite electrodes and AWIS electrolyte showed the highest energy density of 57.2 $W h kg^{-1}$ and maximum power density of 27.6 $kW kg^{-1}$ which is much higher than the previously reported activated carbon/2D material composite based supercapacitors. After 10000 cycles of continuous charging and discharging at 5 $A g^{-1}$ current density, the symmetrical supercapacitor still retained 92.8% of its capacitance, demonstrating excellent cyclic stability of the ACH–900/S composite based supercapacitor. Interestingly, the symmetric supercapacitor fabricated with the siloxene coupled activated carbon electrodes in AWIS electrolyte can operate well in a wide temperature range of 0 °C to 100 °C. In all, this work opens up new frontiers to develop low-cost safe supercapacitors with superior electrochemical performance and wide temperature tolerance.

Author Contributions

RKKR designed, carried out and analyzed most of the practical work and drafted the manuscript. LŠ performed the XPS measurements and assisted with data fitting. AI conceptualized and directly supervised the work and helped in interpreting the results. AI and LŠ provided inputs to the manuscript.

Acknowledgements

AI gratefully acknowledges Scottish Funding Council (SFC) Global Challenges Research Fund (GCRF) and Strathclyde Centre for Doctoral Training (SCDT), Centre for Interdisciplinary Sustainable Practices of Research in Energy (C–INSPRE), for co-funding Kiran's studentship and this project. She also gratefully acknowledges UK Research and Innovation (UKRI), Engineering and Physical Sciences Research Council (EPSRC) for the Fellowship grant (EP/P011500/1). LŠ would like to thank Engineering and Physical Sciences Research Council (EPSRC) UK, for NEXUS facility at Newcastle University (NS/A000015/1). The authors would like to thank Dr. Andrew Callander and Dr. Paul Edwards from University of Strathclyde for assistance in Raman and FESEM measurements, respectively. The authors would like to thank Aaron Naden from University of St. Andrews for HRTEM measurements.

Conflict of Interests

The authors declare no competing interests or personal relationships that could have appeared to influence the work reported in this paper.

Data Availability Statement

The data that support the findings of this study are available from the corresponding author upon reasonable request.

Keywords: activated carbon · corn husk · energy storage · supercapacitors · water-in-salt electrolytes

[1] M. A. Azam, N. S. N. Ramli, N. A. N. M. Nor, T. I. T. Nawi, *Int. J. Energy Res.* **2021**, *45*, 8335–8346.
[2] V. Kumaravel, J. Bartlett, S. C. Pillai, *Adv. Energy Mater.* **2021**, *11*, 2002869.
[3] J. H. Lee, J. S. Chae, J. H. Jeong, H.-J. Ahn, K. C. Roh, *Chem. Commun.* **2019**, *55*, 15081–15084.
[4] L. Peng, Y. Liang, J. Huang, L. Xing, H. Hu, Y. Xiao, H. Dong, Y. Liu, M. Zheng, *ACS Sustainable Chem. Eng.* **2019**, *7*, 10393–10402.
[5] Z. Song, H. Duan, D. Zhu, Y. Lv, W. Xiong, T. Cao, L. Li, M. Liu, L. Gan, *J. Mater. Chem. A* **2019**, *7*, 15801–15811.
[6] L. Sun, Q. Fu, C. Pan, *J. Hazard. Mater.* **2021**, *410*, 124565.
[7] S.-W. Xu, M.-C. Zhang, G.-Q. Zhang, J.-H. Liu, X.-Z. Liu, X. Zhang, D.-D. Zhao, C.-L. Xu, Y.-Q. Zhao, *J. Power Sources* **2019**, *441*, 227220.
[8] K. K. R. Reddygunta, A. Callander, L. Šiller, K. Faulds, L. Berlouis, A. Ivaturi, *Int. J. Energy Res.* **2022**, *46*, 16512–16537.
[9] Y. Sun, Y. Yuan, X. Geng, C. Han, S. Lu, I. Mitrovic, L. Yang, P. Song, C. Zhao, *Carbon.* **2022**, *199*, 224–232.
[10] L. Guardia, L. Suárez, N. Querejeta, V. Vretenár, P. Kotrusz, V. Skákalová, T. A. Centeno, *Electrochim. Acta* **2019**, *298*, 910–917.
[11] L. Wei, W. Deng, S. Li, Z. Wu, J. Cai, J. Luo, *J. Bioresour. Bioprod.*. **2022**, *7*, 63–72.
[12] K. T. Kumar, M. J. K. Reddy, G. S. Sundari, S. Raghu, R. Kalaivani, S. H. Ryu, A. Shanmugharaj, *J. Power Sources* **2020**, *450*, 227618.
[13] Q. Meng, C. Du, Z. Xu, J. Nie, M. Hong, X. Zhang, J. Chen, *Chem. Eng. J.* **2020**, *393*, 124684.
[14] K. Krishnamoorthy, P. Pazhamalai, S.-J. Kim, *Energy Environ. Sci.* **2018**, *11*, 1595–1602.
[15] X. He, X. Zhang, *J. Energy Storage* **2022**, *56*, 106023.
[16] J. Park, J. Lee, W. Kim, *ACS Energy Lett.* **2022**, *7*, 1266–1273.
[17] Q. Ruan, M. Yao, D. Yuan, H. Dong, J. Liu, X. Yuan, W. Fang, G. Zhao, H. Zhang, *Nano Energy.* **2022**, *106*, 108087.
[18] P. M. Yeletsky, M. V. Lebedeva, V. A. Yakovlev, *J. Energy Storage* **2022**, *50*, 104225.
[19] C. Zhong, Y. Deng, W. Hu, J. Qiao, L. Zhang, J. Zhang, *Chem. Soc. Rev.* **2015**, *44*, 7484–7539.
[20] X. Tian, Q. Zhu, B. Xu, *ChemSusChem.* **2021**, *14*, 2501–2515.
[21] L. Suo, O. Borodin, T. Gao, M. Olguin, J. Ho, X. Fan, C. Luo, C. Wang, K. Xu, *Science.* **2015**, *350*, 938–943.
[22] P. Lannelongue, R. Bouchal, E. Mourad, C. Bodin, M. Olarte, S. Le Vot, F. Favier, O. Fontaine, *J. Electrochem. Soc.* **2018**, *165*, A657.
[23] M. Pang, S. Jiang, J. Zhao, S. Zhang, R. Wang, N. Li, R. Liu, Q. Pan, W. Qu, B. Xing, *RSC Adv.* **2020**, *10*, 35545–35556.
[24] G. Hasegawa, K. Kanamori, T. Kiyomura, H. Kurata, T. Abe, K. Nakanishi, *Chem. Mater.* **2016**, *28*, 3944–3950.
[25] J. Yan, D. Zhu, Y. Lv, W. Xiong, M. Liu, L. Gan, *Chin. Chem. Lett.* **2020**, *31*, 579–582.
[26] X. Bu, L. Su, Q. Dou, S. Lei, X. Yan, *J. Mater. Chem. A* **2019**, *7*, 7541–7547.
[27] Q. Dou, Y. Lu, L. Su, X. Zhang, S. Lei, X. Bu, L. Liu, D. Xiao, J. Chen, S. Shi, *Energy Storage Mater.* **2019**, *23*, 603–609.
[28] M. Yu, Y. Lu, H. Zheng, X. Lu, *Chem. Eur. J.* **2018**, *24*, 3639–3649.
[29] X. Fan, L. Chen, O. Borodin, X. Ji, J. Chen, S. Hou, T. Deng, J. Zheng, C. Yang, S.-C. Liou, *Nat. Nanotechnol.* **2018**, *13*, 715–722.
[30] A. Khosrozadeh, L. Tao, P. Zhao, M. B. Miller, O. Voznyy, J. Liu, *J. Power Sources* **2021**, *498*, 229905.
[31] Q. Dou, S. Lei, D.-W. Wang, Q. Zhang, D. Xiao, H. Guo, A. Wang, H. Yang, Y. Li, S. Shi, *Energy Environ. Sci.* **2018**, *11*, 3212–3219.
[32] K. Yu, H. Zhu, H. Qi, C. Liang, *Diamond Relat. Mater.* **2018**, *88*, 18–22.
[33] Y. Wang, J. Sun, X. Qian, Y. Zhang, L. Yu, R. Niu, H. Zhao, J. Zhu, *J. Power Sources* **2019**, *414*, 540–546.
[34] M. Girirajan, N. B. Alagarsamy, K. Ramachandran, R. P. Manimuthu, D. Pazhanivel, K. K. Muthusamy, S. Sakkarapani, *Electrochim. Acta* **2022**, *426*, 140838.
[35] S. Kumar, Y.-P. Fu, *Sustain. Energy Fuels* **2021**, *5*, 3987–4001.

[36] A. Siddiqa, D. Sushmitha, K. Nagaraja, D. Nagaraju, M. Padaki, *J. Electron. Mater.* **2023**, *52*, 1717–1729.
[37] J. Bai, S. Mao, F. Guo, R. Shu, S. Liu, K. Dong, Y. Yu, L. Qian, *New J. Chem.* **2022**, *46*, 10752–10764.
[38] Z. Sun, M. Zheng, H. Hu, H. Dong, Y. Liang, Y. Xiao, B. Lei, Y. Liu, *Chem. Eng. J.* **2018**, *336*, 550–561.
[39] R. Ramachandran, X. Leng, C. Zhao, Z.-X. Xu, F. Wang, *Appl.Mater. Today.* **2020**, *18*, 100477.
[40] R. Ramachandran, M. Li, C. Ge, Z.-X. Xu, F. Wang, in *A selective electrochemical dopamine sensor based on siloxene nanosheet*, Vol. (Ed. Eds.: Editor), IEEE, City, **2020**, pp.295–298.
[41] M. Li, R. Ramachandran, T. Sakthivel, F. Wang, Z.-X. Xu, *Chem. Eng. J.* **2021**, *421*, 129728.
[42] D. Zhang, B. Yang, W. She, S. Gao, J. Wang, Y. Wang, K. Wang, H. Li, L. Han, *J. Power Sources* **2021**, *506*, 230103.
[43] D. Jain, J. Kanungo, S. Tripathi, *J. Alloys Compd.* **2020**, *832*, 154956.
[44] F. Ran, X. Yang, X. Xu, S. Li, Y. Liu, L. Shao, *Chem. Eng. J.* **2021**, *412*, 128673.
[45] Y. Luo, X. Li, X. Hao, Y. Xu, S. Tang, K. Zhang, A. Qin, *J. Energy Storage* **2023**, *67*, 107463.
[46] X. Jiang, G. Shi, G. Wang, P. Mishra, J. Du, Y. Zhang, *Ionics.* **2020**, *26*, 4039–4051.
[47] H. Shen, Y. Zhang, X. Song, Y. Liu, H. Wang, H. Duan, X. Kong, *J. Alloys Compd.* **2019**, *770*, 926–933.
[48] D. J. Arnot, W. Li, D. C. Bock, C. A. Stackhouse, X. Tong, A. R. Head, E. S. Takeuchi, K. J. Takeuchi, S. Yan, L. Wang, *Adv. Mater. Interfaces* **2022**, *9*, 2102238.
[49] K. Krishnamoorthy, P. Pazhamalai, V. K. Mariappan, S. Manoharan, D. Kesavan, S. J. Kim, *Adv. Funct. Mater.* **2021**, *31*, 2008422.
[50] B. J. Ryan, M. P. Hanrahan, Y. Wang, U. Ramesh, C. K. Nyamekye, R. D. Nelson, Z. Liu, C. Huang, B. Whitehead, J. Wang, *Chem. Mater.* **2019**, *32*, 795–804.
[51] E. Zhang, Z. Hu, X. Liu, J. Tang, J. Guo, Y. Zhou, Z. Li, *J. Alloys Compd.* **2023**, *947*, 169489.
[52] K. Fic, G. Lota, M. Meller, E. Frackowiak, *Energy Environ. Sci.* **2012**, *5*, 5842–5850.
[53] H. Feng, H. Hu, H. Dong, Y. Xiao, Y. Cai, B. Lei, Y. Liu, M. Zheng, *J. Power Sources* **2016**, *302*, 164–173.
[54] Y. Yuan, Y. Sun, Z. Feng, X. Li, R. Yi, W. Sun, C. Zhao, L. Yang, *Materials.* **2021**, *14*, 318.
[55] N. Mahato, T. Sreekanth, K. Yoo, J. Kim, *Molecules.* **2023**, *28*, 1520.
[56] M. A. A. Mohd Abdah, N. H. N. Azman, S. Kulandaivalu, Y. Sulaiman, *Sci. Rep.* **2019**, *9*, 16782.
[57] M. P. Adhikari, R. Adhikari, R. G. Shrestha, R. Rajendran, L. Adhikari, P. Bairi, R. R. Pradhananga, L. K. Shrestha, K. Ariga, *Bull. Chem. Soc. Jpn.* **2015**, *88*, 1108–1115.
[58] G. Shi, H. Zhang, Y. Dong, Q. Zhang, Z. Wang, X. Jiang, Y. Hu, F. Luo, X. Li, G. Wang, *Int. J. Electrochem. Sci.* **2019**, *14*, 7608–7622.
[59] X. Yue, H. Yang, Y. Cao, L. Jiang, H. Li, F. Shi, J. Liu, *J. Mater. Sci.* **2022**, *57*, 3645–3661.
[60] D. R. Lobato-Peralta, E. Duque-Brito, H. O. Orugba, D. Arias, A. K. Cuentas-Gallegos, J. A. Okolie, P. U. Okoye, *Diamond Relat. Mater.* **2023**, *138*, 110176.
[61] M. Kigozi, R. Kali, A. Bello, B. Padya, G. M. Kalu-Uka, J. Wasswa, P. K. Jain, P. A. Onwualu, N. Y. Dzade, *Materials.* **2020**, *13*, 5412.
[62] C. J. Raj, R. Manikandan, M. Rajesh, P. Sivakumar, H. Jung, S. J. Das, B. C. Kim, *J. Power Sources* **2021**, *490*, 229518.
[63] K. Surya, M. Michael, *J. Electroanal. Chem.* **2020**, *878*, 114674.
[64] R. Ren, Y. Zhong, X. Ren, Y. Fan, *RSC Adv.* **2022**, *12*, 25807–25814.
[65] M. Hu, T. Hu, R. Cheng, J. Yang, C. Cui, C. Zhang, X. Wang, *J. Energy Chem.* **2018**, *27*, 161–166.
[66] R. Kötz, M. Carlen, *Electrochim. Acta* **2000**, *45*, 2483–2498.
[67] K. K. R. Reddygunta, R. Beresford, L. Šiller, L. Berlouis, A. Ivaturi, *Energy Fuels.* **2023**, *37*, 19248–19265.
[68] W. Yang, Y. Li, Y. Feng, *Materials.* **2018**, *11*, 2455.
[69] L. Yu, L. Hu, B. Anasori, Y.-T. Liu, Q. Zhu, P. Zhang, Y. Gogotsi, B. Xu, *ACS Energy Lett.* **2018**, *3*, 1597–1603.
[70] D. Momodu, N. F. Sylla, B. Mutuma, A. Bello, T. Masikhwa, S. Lindberg, A. Matic, N. Manyala, *J. Electroanal. Chem.* **2019**, *838*, 119–128.
[71] Y. Li, C. Pan, P. Kamdem, X.-J. Jin, *Energy Fuels* **2020**, *34*, 10120–10130.
[72] F. Lai, J. Feng, T. Heil, Z. Tian, J. Schmidt, G.-C. Wang, M. Oschatz, *J. Mater. Chem. A* **2019**, *7*, 19342–19347.
[73] S. Li, Q. Tian, J. Chen, Y. Chen, P. Guo, C. Wei, P. Cui, J. Jiang, X. Li, Q. Xu, *Chem. Eng. J.* **2023**, *457*, 141265.

Manuscript received: March 17, 2024
Revised manuscript received: May 3, 2024
Version of record online: September 10, 2024